

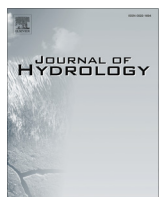


ELSEVIER

Contents lists available at ScienceDirect

Journal of Hydrology

journal homepage: www.elsevier.com/locate/jhydrol



Research papers

Multi-year atmospheric forcing datasets for hydrologic modeling in regions of complex terrain – Methodology and evaluation over the Integrated Precipitation and Hydrology Experiment 2014 domain



Jing Tao, Ana P. Barros *

Department of Civil & Environmental Engineering, Pratt School of Engineering, Duke University, Durham, NC 27708, United States

ARTICLE INFO

Article history:

Received 13 September 2016
Received in revised form 1 December 2016
Accepted 31 December 2016
Available online 9 January 2017
This manuscript was handled by K. Georgakakos, Editor-in-Chief, with the assistance of Jianzhong Wang, Associate Editor

Keywords:

Atmospheric forcing
Downscaling
Hydrologic modeling
Complex topography
Surface energy budget

ABSTRACT

A framework to derive high-resolution long-term meteorological forcing for hydrologic models from mesoscale atmospheric reanalysis products is presented, including topographic and cloud corrections, and a new physical parameterization of near-surface wind fields. The methodology is applied to downscale 3-hourly North American Regional Reanalysis (NARR) fields originally at 32 km spacing to 1 km and hourly resolution for a seven-year period (2007–2013) over the Integrated Precipitation and Hydrology Experiment 2014 (IPHEX2014) domain with the focus on the Southern Appalachian Mountains (SAM) in the SE US. Evaluation of the adjusted downscaled products was conducted against flux tower observations in the IPHEX domain. At high elevations, the Root Mean Squared Errors (RMSEs) of atmospheric pressure decreased from 44.71 to 2.78 hPa, and the RMSEs of near-surface temperature improved by 1 K (up to 5 K in winter). In addition, RMSEs decreased by as much as 100% for near-surface winds (10 m above ground) at all tower locations and by 25–30 W/m² for shortwave radiation at low elevations. Using the uncalibrated Duke Coupled surface-groundwater Hydrology Model (DCHM), the value and utility of the downscaled products for hydrologic offline simulations are demonstrated through comparative analysis of the sensitivity of water and energy budgets in mountain watersheds for four water-years (2007/10–2011/09) including a severe drought and several flood events. Cloud and topographic corrections applied to incoming solar radiation result in hourly net radiation changes ranging from 200 to 500 Wm⁻² at mid-day for clear-sky and cloudy conditions, respectively. Improvements in shortwave radiation and near-surface wind speed estimates have the highest impact on evapotranspiration and soil surface temperature. Wind speed differences of 2–10 m/s translate into basin-averaged differences mid-day surface fluxes up to 300 Wm⁻² and 100 Wm⁻² in the inner SAM, for sensible and latent heat respectively.

© 2017 Elsevier B.V. All rights reserved.

1. Introduction

Numerical Weather Prediction (NWP) reanalysis products that result from optimal merging of model and observations using data assimilation techniques such as atmospheric pressure, incoming radiation (shortwave/solar radiation and longwave/thermal radiation), and air temperature, wind velocity, and specific humidity in the boundary layer, are widely used as a source of atmospheric forcing for hydrological modeling studies. However, significant biases, and also physical inconsistencies in reanalysis products have been reported in the literature, especially in topographically complex regions (Berg et al., 2003; Decker et al., 2012; Kumar

and Merwade, 2011; Maurer et al., 2001; Roads and Betts, 2000; Wang and Zeng, 2012; Zhao et al., 2008). Forced with incorrect meteorology, hydrological models cannot produce reasonable and realistic simulations of the surface water and energy budgets. Furthermore, model calibration using incorrect meteorological forcing can lead to unphysical parameter estimates and unrealistic model behavior for long-term simulations. Errors can be further amplified when there is a large scale gap between the spatial resolution of mesoscale reanalysis products (typically tens of kilometers) and the spatial resolution of hydrological models necessary in mountainous regions (e.g. ≤ 1 km). Therefore, selecting an appropriate downscaling methodology to bridge the resolution gap while preserving key physical constraints is critical to hydrologic modeling studies.

* Corresponding author.

E-mail address: barros@duke.edu (A.P. Barros).

Simple methodologies like bias correction of reanalysis data, and in particular precipitation, can significantly improve the simulations of fluxes in high-resolution hydrologic models compared to observations (Berg et al., 2003; Hay and Clark, 2003; Lenters et al., 2000). Berg et al. (2003) reported that the implementation of a physically-based bias reduction scheme to air temperature, dew point temperature, surface pressure, precipitation, shortwave and longwave radiation from the ECMWF (European Centre for Medium Range Weather Forecast) 15-year reanalysis (ERA) and the National Center for Environmental Prediction/National Center for Atmospheric Research (NCEP/NCAR) reanalysis (NRA) lead to improvements in the correlation coefficients between runoff estimates and observations from 0.29 to 0.68 using a catchment-based land surface model (CLSM); they attributed the improvement to improved precipitation forcing. Other downscaling efforts have focused on producing spatially and temporally consistent retrospective forcing data sets such as the North American Land Data Assimilation System (NLDAS) Land Surface Models (LSMs) at 0.125° resolution (~12.5 km), a valuable resource widely used by the broad community. For NLDAS, Cosgrove et al. (2003) applied a sequential correcting procedure to the NCEP (National Center for Environmental Prediction) Eta Data Assimilation System (EDAS) output fields to account for the topographic difference between NLDAS and EDAS/Eta terrain, adjusting the 2 m air temperature albeit fixing the lapse rate to the global mean standard (~6.5 K/km). Ngo-Duc et al. (2005) followed the NLDAS approach to construct a 53-year meteorological data set for coarse resolution LSMs (~100 km) by interpolating and correcting the NCEP/NCAR (National Center for Atmospheric Research) reanalysis data using a fixed standard lapse rate also. Zhao et al. (2008) followed the same approach to adjust the 2 m surface temperature of NCEP/NCAR reanalysis products and the ERA-40 (ECMWF Reanalysis, European Center for Medium Range Weather Forecasts) in China

Table 1
DOIs and links for datasets developed for IPHEX-H4SE.

| Data sets | DOIs | Link |
|---------------------------|----------------------|---|
| Atmospheric Forcing Data | 10.7924/ G8RN3S6 | http://dukespace.lib.duke.edu/dspace/handle/10161/8958 |
| Precipitation | 10.7924/ G8MW2F2W | http://dukespace.lib.duke.edu/dspace/handle/10161/8969 |
| Landscape Attributes Data | 10.7924/ G8H41PBG | http://dukespace.lib.duke.edu/dspace/handle/10161/8968 |

and reported average reductions of 43.6% in the standard deviation of summertime surface temperature bias compared against observations in mountainous regions. Recently, Gao et al. (2012) applied an elevation correction method to downscale ERA-Interim air temperature data in complex terrain using vertical lapse rates derived from different pressure levels, and demonstrated that using dynamic lapse rates significantly improved the downscaling performance compared to using the standard (fixed) lapse rate. Schomburg et al. (2010) proposed an alternative approach to downscale atmospheric model output using bilinear interpolation and local empirical relationships among surface properties, topography, and the mean values and anomalies of atmospheric near-surface variables simulated by the same models in the region of interest, that is the “modeled hydroclimate”. This approach implies a priori calibration of the relationships between surface properties and near-surface atmospheric variables to capture their variability at the desired spatial resolution. The calibrated relationships depend on the atmospheric model and the specific model configuration, and thus cannot be transferred or applied generally.

In this manuscript, we present the development of high-resolution atmospheric forcing datasets for hydrological modeling (1 km, hourly) from the North American Regional Reanalysis (NARR) products, originally at 32 km spatial resolution and 3-hourly temporal resolution (Mesinger et al., 2006), including radi-

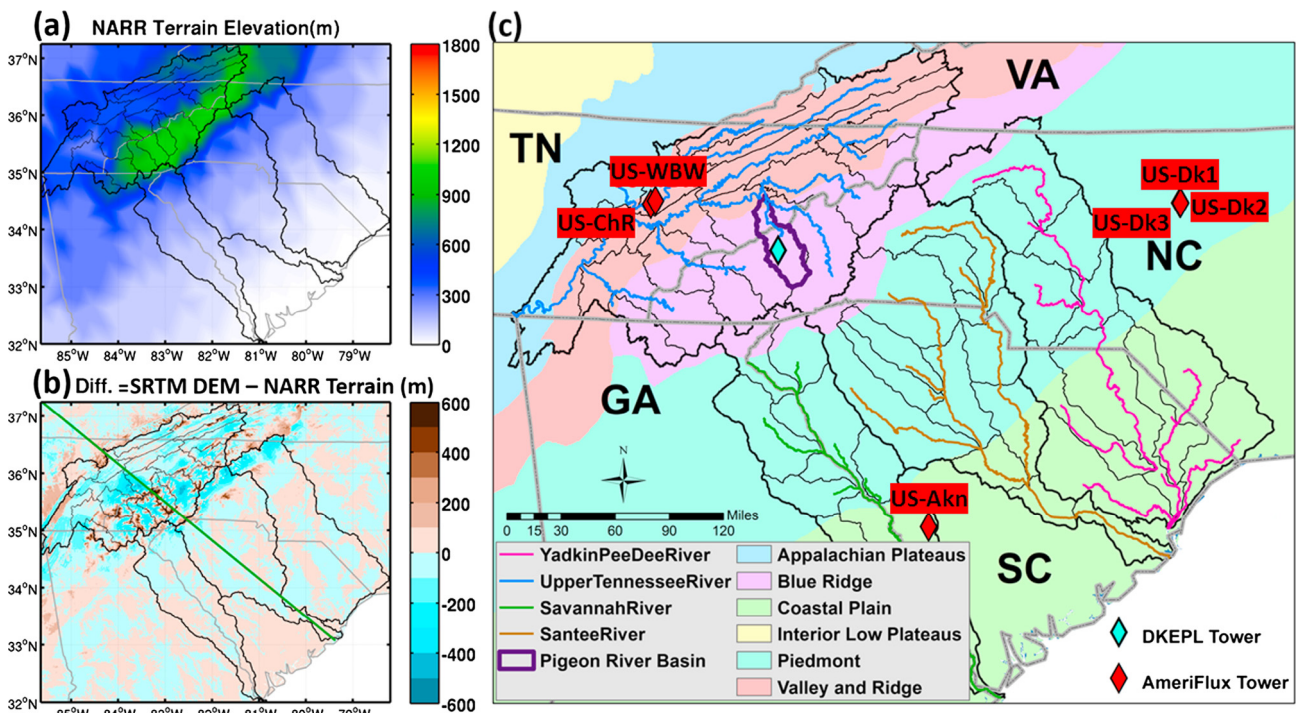


Fig. 1. NARR terrain elevation bi-linearly interpolated from 32 km to 1 km (a), the elevation difference between the Shuttle Radar Topography Mission(SRTM) DEM and the NARR terrain (b); the green NW-SE transect line marked in (b) is used to illustrate the elevation correction in Fig. 3; panel (c) shows the physiographic provinces, the Pigeon River Basin outlined in purple (PRB), and the AmeriFlux (red diamonds) and the Duke Environmental Physics Laboratory (DKEPL, green diamond) tower locations. (For interpretation of the references to color in this figure legend, the reader is referred to the web version of this article.)

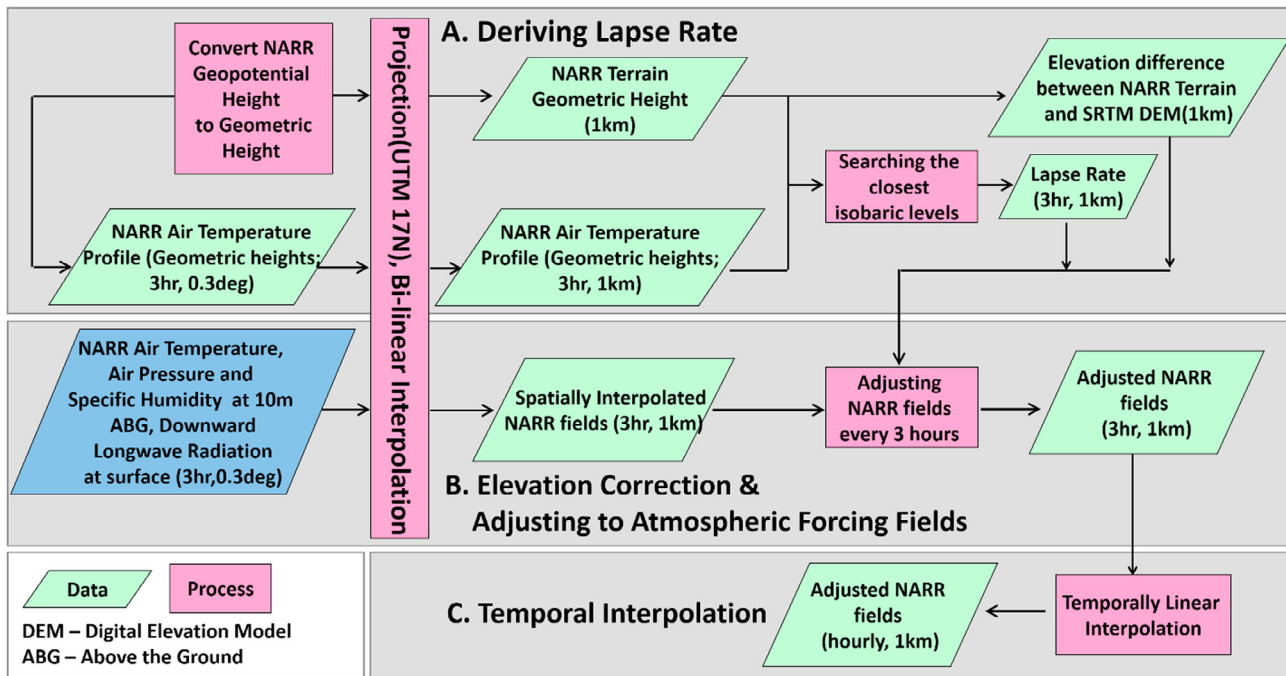


Fig. 2. Flowchart for elevation correction to NARR air temperature, air pressure, specific humidity and downward longwave radiation. Blue represents the original data; green represents the intermediate or processed results; the pink rectangles indicate specific actions. (For interpretation of the references to color in this figure legend, the reader is referred to the web version of this article.)

ation fluxes, atmospheric temperature, atmospheric pressure, wind velocity, and specific humidity at 10 m above ground (ABG). The precipitation forcing is obtained from the NCEP/EMC 4 km Gridded Data (GRIB) Stage IV dataset down-scaled to 1 km using multifractal methods (Nogueira and Barros, 2014a, 2015). Whereas high-quality long-term mesoscale resolution reanalysis products such as NARR will not be available outside of the US, the methodology is applicable to NWP and RCM (Regional Climate Model) simulations generally.

The impetus to derive these data sets in preparation for IPHEX2014 was to provide consistent forcing for hydrologic models at high temporal resolution, including operational hydrologic forecasting in regions of complex terrain generally, and the Southern Appalachian Mountains in particular (Barros et al., 2014; Tao et al., 2016; <http://iphex.pratt.duke.edu>). Therefore, a deliberate effort was made to capture the diurnal cycle as well as seasonal and inter-annual variability consistent with regional hydroclimate. The IPHEX spatial domain spans four macro-scale river basins of interest with headwaters in the Southern Appalachians (Fig. 1): the Upper Tennessee River Basin (UTRB), the Savannah River Basin (SVRB), the Catawba-Santee River Basin (CSR) and the Yadkin-Pee Dee River Basin (YPDRB). Further information can be found in the IPHEX2014 science plan (Barros et al., 2014). The final data set consisting of 7 years of corrected and down-scaled atmospheric forcing data (2007–2013) at hourly time-scales and 1 km resolution is publicly available from Duke University Libraries (see Table 1). Quality landscape attributes at consistent spatial and temporal resolution to specify hydrologic model parameters were also produced and made publicly available (Tao and Barros, 2014b). The present manuscript is organized as follows. Section 2 describes the key elements of the methodology. The down-scaled products are evaluated in Section 3, and the impact of the corrected atmospheric forcing products on hydrologic simulations is discussed in Section 4. Section 5 provides a summary of the work.

2. Downscaling methodology and corrections

2.1. Synopsis

The dynamic lapse rates were derived from the NARR atmospheric temperature profiles using the isobaric levels closest to the NARR terrain and the local terrain at 1 km, and then were applied to correct atmospheric temperature first, followed by air pressure, specific humidity and longwave radiation (Section 2.2). To downscale the wind velocity from the NARR coarse resolution to 1 km, the friction velocity is down-scaled using a new parameterization based on an heuristic relationship between the geostrophic drag coefficients and the Rossby number suggested by Lettau (1959), and the surface wind speed was adjusted subsequently using the down-scaled friction velocity as well as surface roughness length at high spatial resolution (Section 2.3).

Accurate real-time (hourly and even more frequent) shortwave radiation at high spatial resolution is essential for hydrological applications, because radiative forcing drives water transfers and energy fluxes and modulates the efficiency of photosynthesis. NARR 3-hourly downward shortwave (SW) radiation shows large bias especially in topographically complex regions (Pinker et al., 2003; Schroeder et al., 2009). To downscale the NARR incoming shortwave radiation to high spatial resolution for this study, cloud and topographic effects are accounted for in real-time to capture the rapid evolution of cloud systems within the complex topography and microclimates of the SAM inner region. This requires the implementation of special corrections for downward shortwave radiation through dynamical adjustment including both cloudiness and topographic effects (Section 2.4).

The NLDAS-2 primary forcing data (Mitchell et al., 2004; Xia et al., 2012a, 2012b) includes bias-corrected NARR downward shortwave radiation using a ratio-based bias correction method at monthly time-scales (Berg et al., 2003). In their approach, the bias ratio was calculated between the monthly mean diurnal cycle

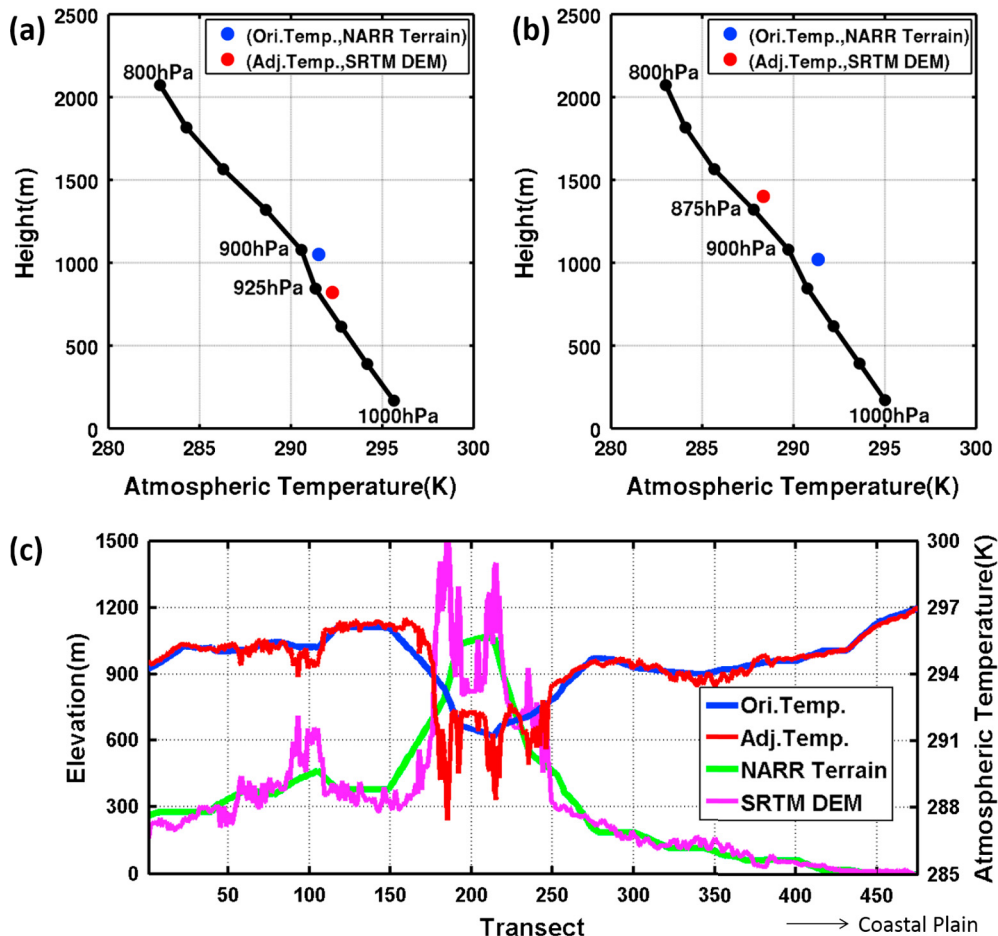


Fig. 3. Example of elevation correction to atmospheric temperature 10 m above ground (ABG) at a pixel where the Shuttle Radar Topography Mission (SRTM) DEM is below the NARR terrain (a), and at a pixel where the SRTM DEM is above (b). Black dots indicate NARR isobaric levels ranging from 800 hPa to 1000 hPa with an interval as 25 hPa. The bottom panel (c) shows the elevation correction along the transect line marked in Fig. 1b.

of downward shortwave radiation from the GEWEX Continental Scale International Project (GCIP) Surface Radiation Budget (SRB) dataset (Pinker et al., 2003) and the NARR monthly mean values, and then applied to correct hourly NARR radiation linearly interpolated in time from the 3-hourly NARR data. Here, the bias corrections are estimated at daily time-scales instead of using monthly means. The methodology follows Dubayah and Loeschel (1997) and relies on the GCIP SRB dataset¹ hereafter referred to as GSRB for retrieving shortwave atmospheric transmittance and real-time cloudiness patterns. The corrections account for regional cloud patterns, cast-shadow caused by sun-blocking terrain, topographic self-shadow, and the reflected shortwave radiation from the surrounding terrain. Note that, after July 2010, the GSRB dataset was discontinued, after which time NARR cloud patterns are used to correct incoming shortwave radiation and this necessarily has an impact on the quality of corrections.

Finally, the NARR products rely heavily on data-assimilation (Mesinger et al., 2006) of multiple types of observations (including remote-sensing). Consideration of scale-dependent scaling of atmospheric variables introduced through data-assimilation (e.g. Sun and Barros, 2010) and, or due to the specific model configuration and implementation (e.g. Nogueira and Barros, 2014b) is out of the scope of this work.

2.2. Elevation corrections

NARR terrain at ~32 km grid spacing is analogous to a smooth envelope of the high resolution topography at ~1 km resolution (Fig. 1a and b), with elevation differences between the NARR terrain and the local (Digital Elevation Model (DEM)) as large as 1064 m along the ridge lines of the Pigeon River Basin. Therefore, the 3-hourly atmospheric pressure, air temperature and specific humidity 10 m above ground (ABG), and downward longwave radiation at the surface must be corrected for topographic discrepancies first. For this purpose, the original NARR fields including the NARR terrain were bi-linearly interpolated to a 1 km grid, and the elevation differences between the NARR terrain and the local 1 km DEM sampled from the Shuttle Radar Topography Mission (SRTM) data² at 90 m spatial resolution were determined. Next, the atmospheric pressure, specific humidity and downward longwave radiation were corrected sequentially.

High-resolution elevation corrections (topographic adjustments) require dynamic lapse rates for adjusting atmospheric temperature. The lapse rate was calculated from the NARR atmospheric temperature profile at low isobaric levels (1000 mb to 800 mb) for each pixel (1 km grid element) at each time step (3-hourly). Instead of using NARR terrain as the reference level, the two closest geometric heights converted from the geopotential

¹ The GCIP SRB data can be obtained from <http://www.atmos.umd.edu/~srb/gcip/>.

² <http://srtm.csi.cgiar.org/SELECTION/inputCoord.asp>.

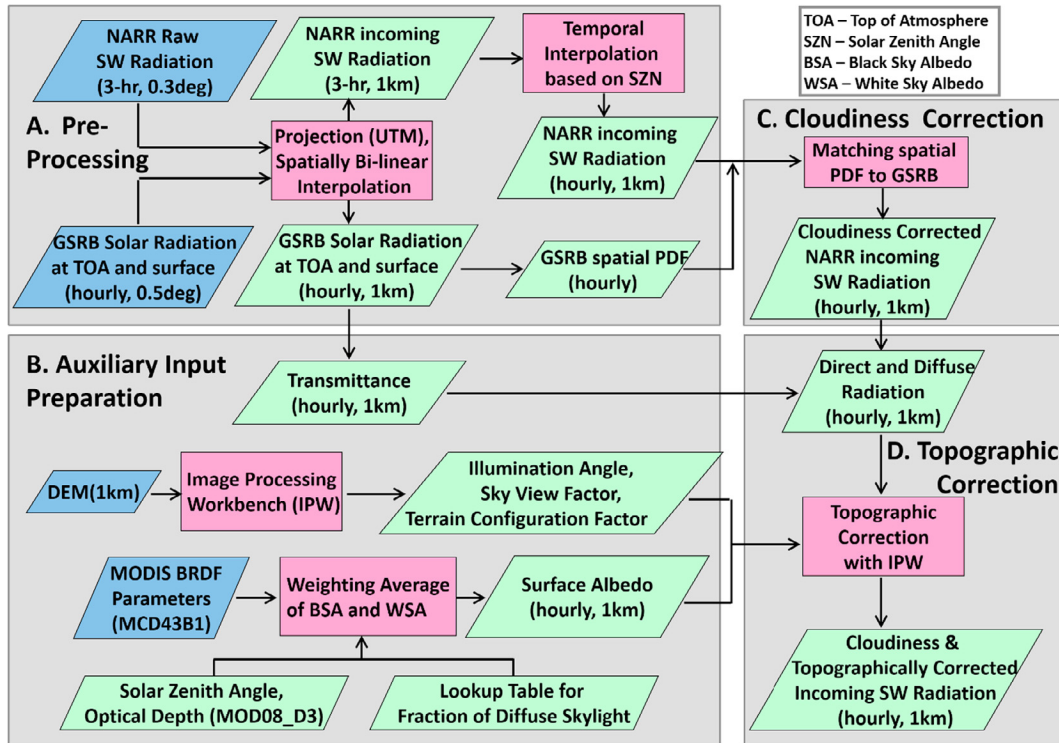


Fig. 4. Flowchart illustrating the work to generate the cloudiness-corrected and topographically corrected hourly shortwave radiation data from NARR 3-hourly shortwave radiation. Color scheme as in Fig. 2. (For interpretation of the references to color in this figure legend, the reader is referred to the web version of this article.)

heights corresponding to the NARR terrain and the local DEM were utilized to calculate the lapse rate in the atmospheric surface layer. The latter is used in turn to adjust atmospheric temperature from the NARR to the local DEM at 1 km. Fig. 2 provides the flowchart describing all intermediate steps in the elevation correction algorithm.

At location s and time t , the adjusted atmospheric temperature is calculated by

$$T_{\text{adj}}(t, s) = T_{\text{NARR}}(t, s) + \gamma(t, s)\Delta z \quad (1)$$

where T_{adj} is the adjusted atmospheric temperature (K) 10 m ABG based on the local terrain at 1 km, T_{NARR} is the original NARR atmospheric temperature (K) 10 m ABG, γ is the dynamic lapse rate (K/km), and Δz is the elevation difference between the NARR terrain and the DEM data at 1 km. The lapse rate γ depends on the atmospheric conditions, time of day and location. Fig. 3 shows an example of lapse rate estimates derived using the elevation correction. In Fig. 3a, the 900 hPa height (the closest level to the NARR terrain) and the 925 hPa height (the closest level to the SRTM DEM) were selected to estimate the lapse rate $\gamma = -3.28 \text{ K/km}$, that is quite different from the standard value (-6.5 K/km) as expected. In Fig. 3b, the SRTM DEM is much higher than the NARR terrain, and the heights and temperatures at 875 hPa and 900 hPa were selected to estimate the lapse rate $\gamma = -7.91 \text{ K/km}$. Fig. 3c demonstrates the application of the elevation correction to the NARR atmospheric temperature along the transect marked in Fig. 1b starting in the Tennessee Valley and crossing the Blue Ridge Mountains into the Coastal Plains. The adjusted surface air temperature fields are very different from the original NARR values in the mountains (up to 6 K) as shown in Fig. 3c. Not surprisingly, the differences in temperature are not very large in the smooth and low elevation topography of the Piedmont and the Coastal Plain due to the small elevation differences between the NARR terrain and the DEM. The adjustments for air pressure, specific humidity 10 m ABG and downward longwave

radiation at the surface follow strictly the procedure described by Cosgrove et al. (2003), and can be found also in the corresponding IPHEx2014 technical report by Tao and Barros (2014c).

2.3. Wind adjustment

For the wind adjustment, we first begin by adjusting the friction velocity based on the dependence of the geostrophic drag coefficient on surface roughness (Lettau, 1959). Two spatial scales of interest are considered: the geostrophic (synoptic) scale L that depends on the pressure gradient force and the Coriolis acceleration, and the mesoscale l that depends on the regional topography (i.e. the roughness length at the scale of interest). The geostrophic drag coefficient at a scale L can be expressed as $C_g = \frac{u_L^*}{U_g}$, where u_L^* is the surface layer friction velocity at scale L , and U_g is the geostrophic wind (it is assumed implicitly that the ageostrophic component of the total wind can be neglected, and thus $U \approx U_g$). Based on balloon measurements, Lettau (1959) proposed an empirical relationship between the geostrophic drag coefficient and the Rossby number R_o as follows:

$$C_g = 0.16R_o^{-0.09} \quad (2)$$

and $R_o = \frac{U_g}{f \times z_{0,L}}$, where f is the Coriolis acceleration and $z_{0,L}$ is the roughness length at scale L . The Rossby number is the ratio of the pressure gradient force (that drives the geostrophic wind) and the Coriolis force at the scale of interest. By replacing R_o in Eq. (2), the following identity is obtained:

$$0.16(U_g)^{0.91} = u_L^*(f \times z_{0,L})^{-0.09} \quad (3)$$

Assuming that the geostrophic wind U_g component of the total wind is the same at the NARR resolution scale L ($=32 \text{ km}$) and at the local scale l ($=1 \text{ km}$), the relationship between the friction velocity at the two scales can be expressed as

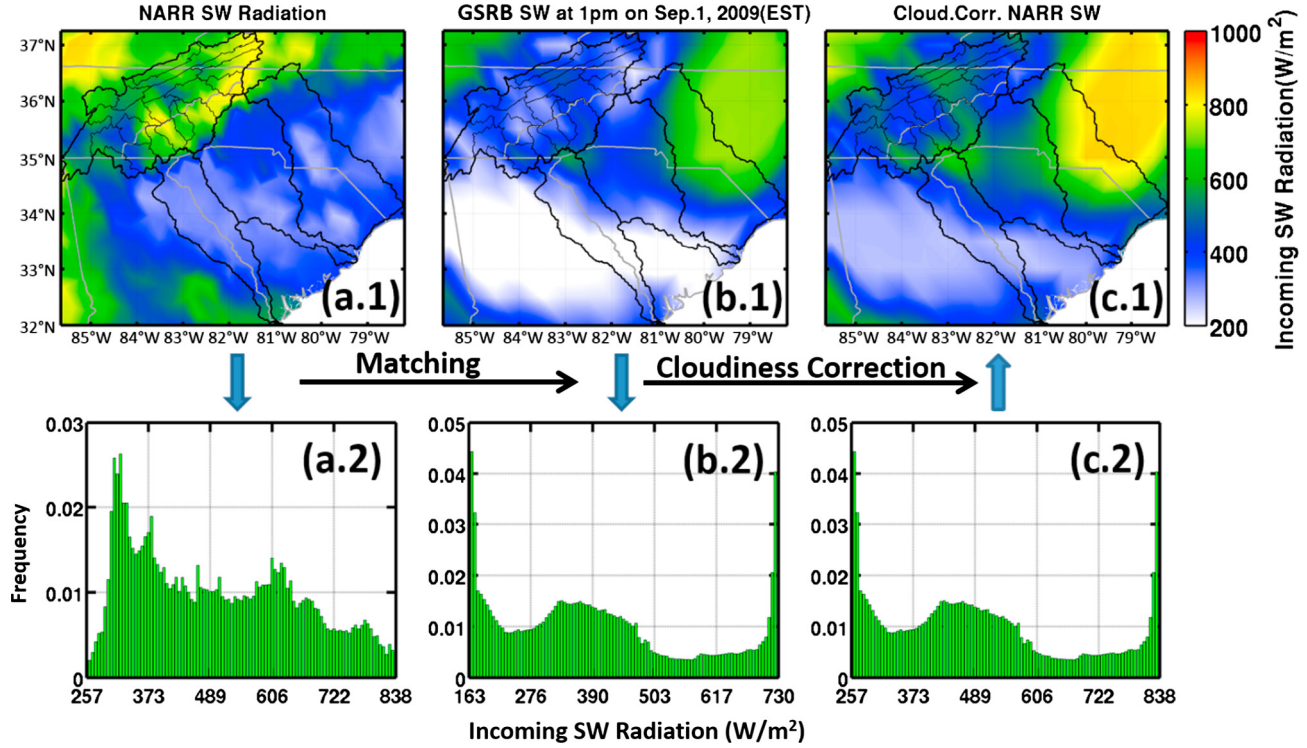


Fig. 5. Example of cloudiness correction applied to NARR SW radiation by matching the spatial PDF to that of GCIP SRB SW data over the SE US at 1 PM (EST) on Sep. 1, 2009.

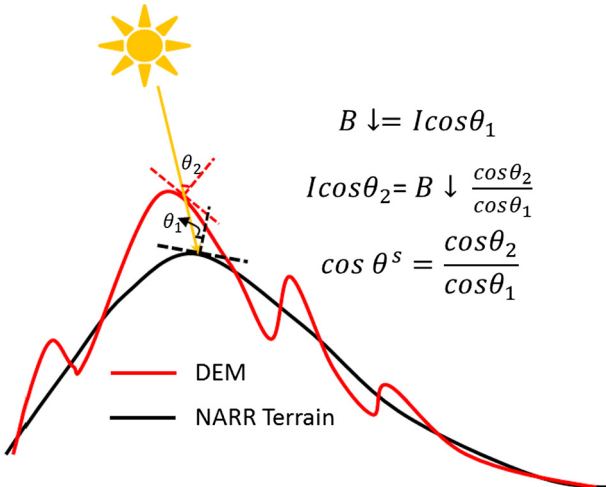


Fig. 6. Difference in the local solar illumination angle caused by the different topography of DEM and NARR terrain. I is the incoming radiation after atmospheric attenuation; $B \downarrow$ is the narr surface direct beam irradiance product already projected on the NARR terrain; θ_1 is the solar illumination angle based on the NARR terrain, and θ_2 is the local solar illumination angle based on the high-resolution DEM. The topographic correction consists of scaling $B \downarrow$ by the ratio of the cosine of θ_2 over the cosine of θ_1 . This ratio is the scaled cosine of the solar illumination angle [$\cos \theta^s$].

$$u_L^*(f \times z_{0,L})^{-0.09} = u_l^*(f \times z_{0,l})^{-0.09} \quad (4)$$

Rearranging the terms above, the friction velocity at scale l can be estimated from the friction velocity at scale L :

$$u_l^* = u_L^* \left(\frac{z_{0,L}}{z_{0,l}} \right)^{-0.09} \quad (5)$$

The roughness length $z_{0,L}$ at scale L is obtained from NARR parameters, and the friction velocity u_L^* is retrieved from the NARR's wind speeds at 10 m and 30 m ABG using the classical

logarithm law approximation of the low-level wind speed profile. In the boundary layer, the adjusted 10 m ABG wind speed at scale l is expressed finally as:

$$U^l = \frac{u_*^l}{k} \log \left(\frac{10 - d}{z_{0,l}} \right) \quad (6)$$

where k is the Von Kármán constant (~ 0.41), and the roughness length $z_{0,l}$ and the displacement height d depend on the land-cover at the same spatial scale (1 km).

This parameterization of friction velocity based on physical scaling arguments aims to capture mesoscale wind shear effects. The dynamics of airflow in complex terrain, including blocking and channelization effects, ridge-valley circulations, or organized convection, which require physically-based modeling of atmospheric flows at the relevant scales, are therefore not represented.

2.4. Topographic and cloudiness correction of downward (Incoming) shortwave radiation

The correction technique includes four distinctly important steps summarized in Fig. 4: (2.4.1) Preprocessing, (2.4.2) Preparation for auxiliary input parameters, (2.4.3) Cloudiness correction, and (2.4.4) Topographic correction.

2.4.1. Preprocessing

The preprocessing mainly involves re-projecting all radiative fluxes to UTM 17N (WGS84) coordinates, followed by bi-linearly interpolation to 1 km resolution. After the spatial interpolation, the NARR SW data are then interpolated in time from 3-hourly to hourly resolution based on the real-time local solar zenith angle. This step is similar to (Cosgrove et al., 2003), but their temporal interpolation method using the solar zenith angle cannot be applied for cloudy conditions. Instead, a two-step modified temporal interpolation is developed to fit a smooth diurnal cycle estimator that preserves the total daily energy SW_{tot} using the original

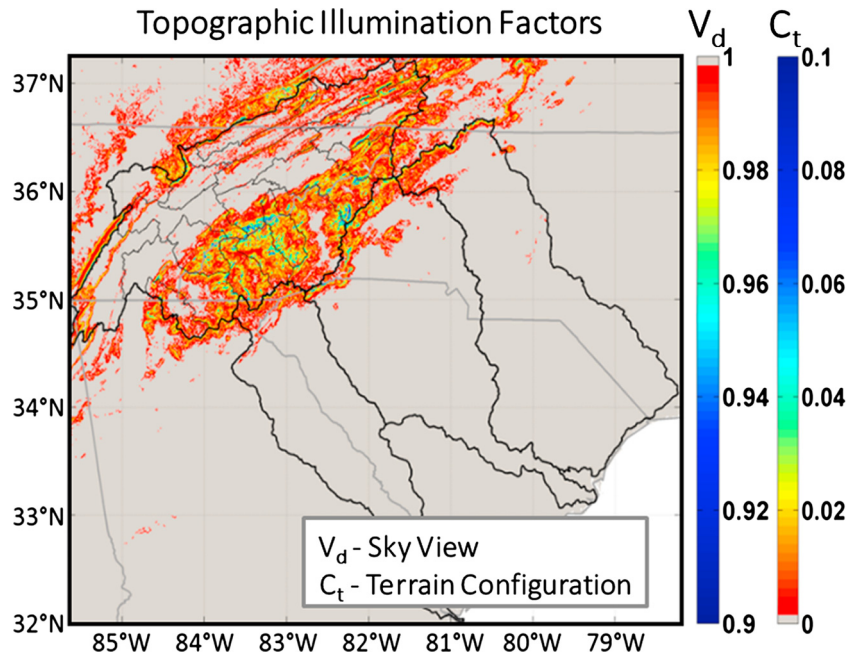


Fig. 7. Topographic illumination factors: Sky View (V_d) and Terrain Configuration (C_t). The topographic illumination factors are fixed auxiliary input parameters in the topographic correction of radiation. C_t scale is adjusted to fit with V_d scale.

Table 2
Landcover at tower locations.

| Station | Lat. | Lon. | Elev. (m) | MODIS Landcover (IGBP) | MODIS Landcover (UMD Type) | Tower footprint |
|-------------|---------|----------|-----------|-----------------------------|-----------------------------|-----------------------|
| US-Akn | 33.3833 | -81.5656 | 92 | Mixed Forest | Mixed Forest | Forest |
| US-ChR | 35.9311 | -84.3324 | 286 | Deciduous Broad-leaf Forest | Deciduous Broad-leaf Forest | Chestnut ridge |
| US-Dk1 | 35.9712 | -79.0934 | 168 | Mixed Forest | Woody Savannas | Grassland, open field |
| US-Dk2 | 35.9736 | -79.1004 | 168 | Mixed Forest | Woody Savannas | Hardwoods |
| US-Dk3 | 35.9782 | -79.0942 | 163 | Mixed Forest | Mixed Forest | Loblolly pine |
| US-WBW | 35.9588 | -84.2874 | 343 | Deciduous Broadleaf Forest | Deciduous Broadleaf Forest | Oak Ridge |
| DKEPL Tower | 35.5877 | -83.0647 | 1486 | Mixed Forest | Mixed Forest | Forest |

3-hourly NARR SW radiation [$SW_i^{NARR}, i = 1, 8$] weighted by the mean cosine of the hourly solar zenith angle for each three-hour period, i.e. $\cos \varphi_i = \frac{1}{3} \sum_{j=1}^3 \cos \varphi_{ij}$, to yield the adjusted local mean three-hourly SW_i radiation:

$$SW_i = SW_{tot} \left(\frac{\sqrt{SW_i^{NARR} \cos \varphi_i}}{\sum_{i=1}^8 \sqrt{SW_i^{NARR} \cos \varphi_i}} \right) \quad (7)$$

The local hourly SW_{ij} radiation is subsequently interpolated from the 3-hourly adjusted NARR SW_i radiation as follows:

$$SW_{ij} = SW_i \left(\frac{\cos \varphi_{ij}}{\sum_{j=1}^3 \cos \varphi_{ij}} \right) \quad (8)$$

where i varies from 1 to 8, 8 is the total daily number of 3-h intervals in the NARR data, and j varies from 1 to 3, indicating the j th hour within each 3-h interval. By incorporating the SW_i^{NARR} term, the hourly shortwave radiation depends on the local solar zenith angle and also on the modification of incoming shortwave radiation due to clouds in NARR. After the temporal interpolation is complete, the cloudiness and topographic corrections are applied to the hourly incoming shortwave radiation (Eq. (8)).

2.4.2. Preparation for auxiliary input parameters

The shortwave transmittance parameter partitions direct and diffuse radiation. Transmittance was calculated using the ratio of the hourly downward solar radiation at the surface to the incoming solar radiation at the top-of-atmosphere (TOA) calculated using GRSB data when available, and from NARR otherwise. The derived transmittance is considered representative of cloudy atmospheric conditions when the solar zenith angle is less than 55°. In reality, highly non-linear relationships exist between transmittance and the cosine solar zenith angle over the full range of solar zenith angles depending on heterogeneous cloud distributions.

The GSRB product does not provide data for early morning and late afternoon for lower values of the cosine of the solar zenith angle, i.e. solar zenith angles larger than 70° (Cosgrove et al., 2003). Consequently, a filling strategy was implemented based on the assumption that the cosine of the solar zenith angle can be approximated to the first order by the shortwave transmittance (Chavez, 1996). This approximation works best at dawn or dusk, when the incoming solar radiation is also very small. The filling steps implemented are as follows: (1) the downward solar radiation at the top-of-atmosphere and at the surface is used to estimate the transmittance; (2) missing values are replaced with the nearest non-missing transmittance multiplied by the ratio of cosine of the solar zenith angle for the pixel where data are missing to the cosine of the solar zenith angle in the nearest-neighbor pixel; (3) temporal filling was performed for the transmittance in early morning and late afternoon using the closest available data, e.g. using transmittance at 9 AM

to fill the missing data in 6 AM ~ 8 AM, also based on the ratio of cosine of the solar zenith angles; and (4) to account for the variability both in space and time, the final transmittance at a given location and time is the average of spatially and temporally filled transmittance. If there are missing data over a large region, only temporal filling is conducted, and the temporally filled transmittance is the final transmittance.

In addition to determining atmospheric transmittance, other auxiliary input parameters such as the sky view factor, the terrain configuration factor, the hourly local illumination angle, and the actual surface albedo must be defined prior to applying the topographic correction for shortwave radiation. Albedo influences the reflected radiation from the surrounding terrain, and the local illumination angle affects the direct radiation received at a slope.

The albedo exhibits large spatial and temporal variability depending on land cover type (i.e. forest, cropland or bare ground) and hydrometeorological conditions (dry/wet), with the amplitude of the diurnal cycle determined by the local fraction of diffuse skylight. The actual albedo of the land surface is a weighted average of the black-sky albedo (BSA) and the white-sky albedo (WSA). The weighting coefficient is the fraction of diffuse skylight depending on solar zenith angle, optical depth, local aerosol type, etc. (Schaaf et al., 2002). Hourly BSA and WSA were calculated using

solar zenith angle and the BRDF (Bidirectional Reflectance Distribution Function) model parameters provided by the MODIS product (MCD43B1) as per Tao and Barros (2014b).

The local illumination angle plays an important role for quantifying the effects of self-shadowing and reducing the incoming direct irradiance when the Sun is below the local horizon of the slope. The cosine of the local illumination angle shows large spatial variability in regions of complex terrain, due to the relative position of the Sun and the local terrain slope. Besides topography, the diurnal variability and seasonal variability in the local illumination angle are determined by the altitude and azimuth of the Sun. The sky view factor represents the total portion of unobstructed sky visible on a slope in all directions, with a value of unity indicating that the sky is unobstructed and zero meaning the sky is completely obstructed by surrounding topography (i.e. the sky view factor is very small at the bottom of a narrow valley because the surrounding terrain blocks diffuse radiation). The terrain configuration factor at a pixel location is the fraction of the hemispheric view that receives reflected radiation from the surrounding terrain. A terrain configuration factor of unity means that only terrain is visible. The methodology to calculate the sky view factor and terrain correction factor is presented in the Topographic Correction Section 2.4.4 below.

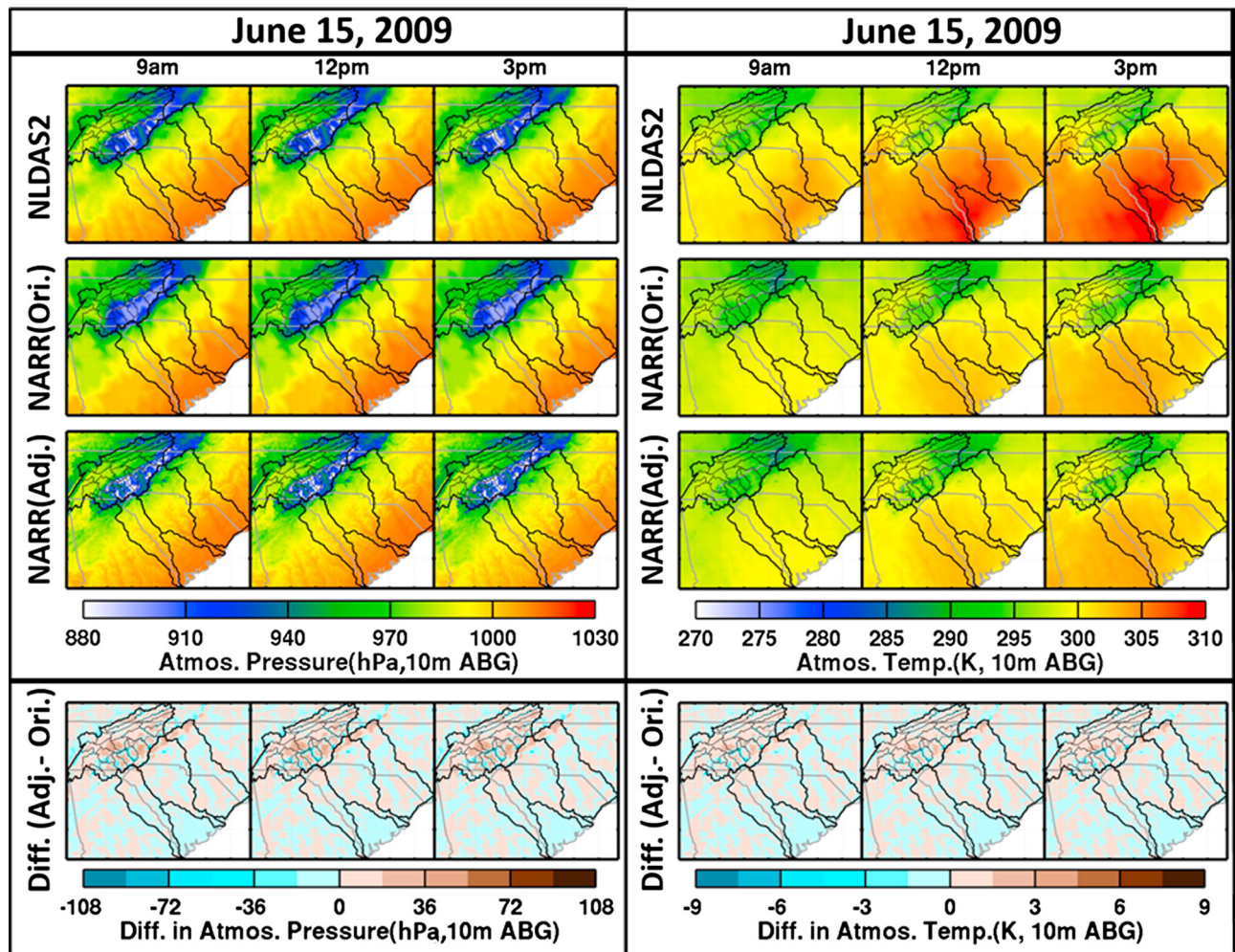


Fig. 8. Atmospheric pressure (left column) and temperature (right column) 10 m above ground (ABG) over the SE US from NLDAS2, NARR before (Ori) and after (Adj) elevation correction/adjustment at 9 AM, noon and 3 PM (EST) on June 15, 2009. The bottom panels show the difference between the NARR atmospheric pressure (left) and temperature (right) after and before adjustment, using a symmetrical blue-brown color scale such that the brown color represents positive values and the blue color represents negative values. The scale captures the full range of the differences for each variable.

2.4.3. Cloudiness correction

In clear-sky conditions, topographic effects dominate the spatial variability of incoming solar radiation. For cloudy conditions, the cloudiness pattern ultimately determines the spatial distribution of the solar radiation. In order to account for real-time cloudiness patterns, the Probability Density Functions (PDFs) of both the spatial GSRB solar radiation and the NARR shortwave radiation are calculated first, and then the PDF of the NARR shortwave radiation is matched to that of the GSRB data by calculating a histogram index at each pixel, $\lambda(i,j) = (R_{max}^S - R^S(i,j)) / (R_{max}^S - R_{min}^S)$ where $R^S(i,j)$ is the GSRB solar radiation at pixel (i,j) , and R_{max}^S and R_{min}^S are the maximum and minimum values of the spatial GSRB solar radiation at the present time, respectively. The regional cloudiness pattern $\lambda(i,j)$ is mapped into a position at the histogram scale. Using the histogram index $\lambda(i,j)$, the NARR SW radiation is reshuffled by

matching its PDF to the GSRB's PDF, such that $R(i,j) = R_{max} - \lambda(i,j)(R_{max} - R_{min})$ where $R(i,j)$ is the NARR SW radiation accounting for the cloudiness pattern, and R_{max} and R_{min} are the maximum and minimum values of the spatial NARR SW radiation at the current time. As it can be seen from Fig. 5, panel (c.2) exhibits the exact same PDF shape as the spatial PDF of GSRB in (b.2), thus the same cloudiness pattern as the GSRB data (c.1 versus b.1), while maintaining the original range of NARR SW radiation (c.2) over the region.

2.4.4. Topographic correction

The topographic correction is applied after the cloudiness correction (C) as indicated by the work flow in Fig. 4. The topographic solar radiation model and the topographic correction used in this study were developed originally by Dozier (1980) and Dozier and Frew (1990) from the simulated total incoming radiation at sea

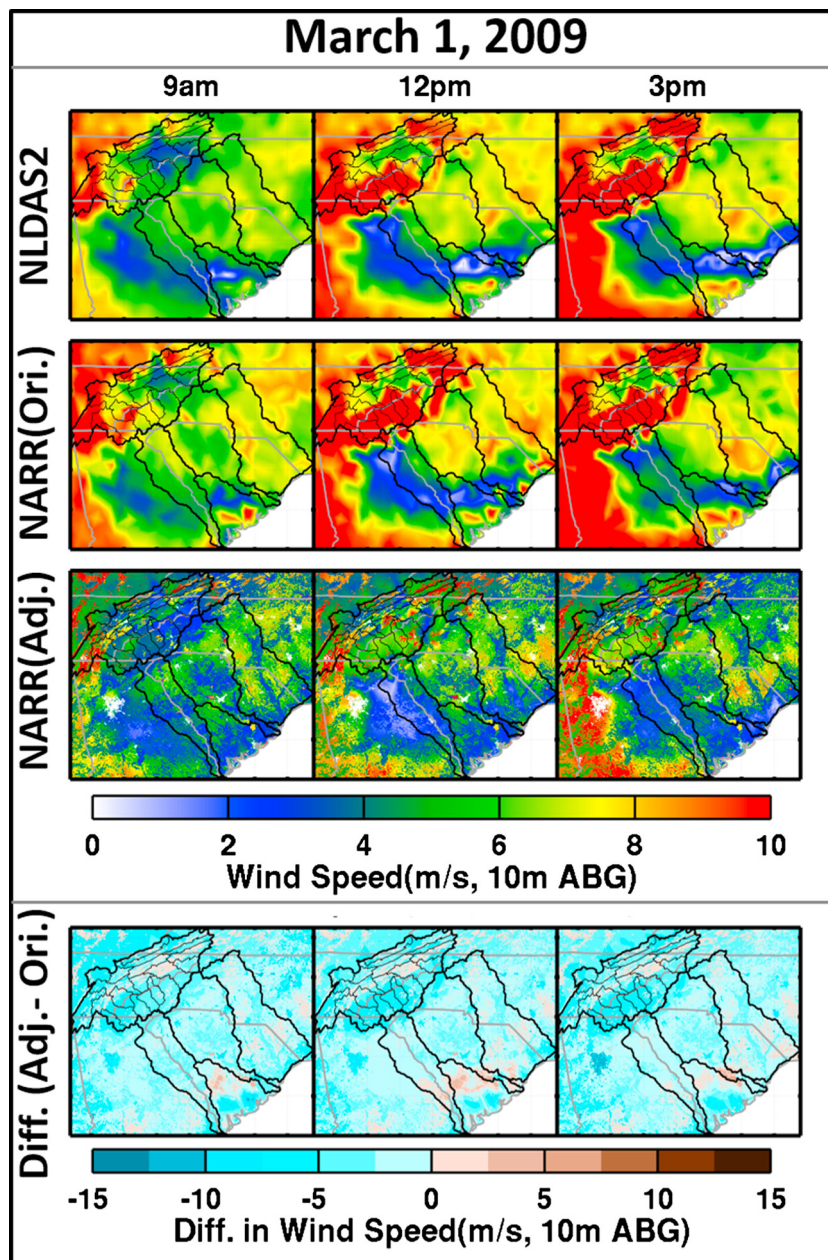


Fig. 9. Comparison of wind speed among NLDAS2, NARR before (Ori) and after (Adj) correction/adjustment at 9AM, noon and 3 PM (EST) on March 1 in 2009. The bottom panels show the difference between the NARR wind speed after and before adjustment.

level. An elevation correction is required before applying the topographic correction to solar radiation in the original model. However, the NARR incoming shortwave radiation is already at the NARR terrain elevation, thus the elevation correction was not implemented. Despite elevation differences between the NARR terrain elevation and the digital elevation model (DEM) at 1 km resolution, we assume that the elevation effects caused by this difference are negligible compared to other topographic effects, such as blocking of the incoming radiation and, or radiation reflection by the surrounding terrain, especially in regions of complex terrain such as the Southern Appalachian mountains. The theoretical basis of the topographic radiation correction is described briefly next.

The total incoming solar radiation consist of three components: the diffuse irradiance from the sky, direct irradiance from the Sun, and diffuse and direct irradiance from nearby terrain (Dubayah and Paul, 1995). The total downward shortwave radiation can be expressed as,

$$SW_{\downarrow tot}(i,j) = F \downarrow(i,j)V_d(i,j) + \delta \cos \theta_{ij}B \downarrow(i,j) + C_t(i,j)F \uparrow(i,j) \quad (9)$$

where $F \downarrow(i,j)$ is the incoming diffuse irradiance, $F \uparrow(i,j)$ is the upwelling (terrain reflected) flux, and $B \downarrow(i,j)$ is the direct beam irradiance; $V_d(i,j)$ is the sky view factor and $C_t(i,j)$ is the terrain configuration factor; δ is a binary shadow mask set equal to either 1 or 0 depending on the shadow caused by nearby terrain blocking the Sun (cast-shadowing); and $\cos \theta_{ij}$ is the cosine of the local solar illumination angle indicating whether the Sun is below or above the local horizon caused by the slope itself (self-

shadowing) [calculated as $\cos \theta_{ij} = \cos \theta_0 \cos S + \sin \theta_0 \sin S \cos (\phi_0 - A)$, where θ_0 is solar zenith angle and ϕ_0 is solar azimuth angle, S and A are slope magnitude and aspect]. The original algorithm performs the topographic correction based on the incoming-atmospheric radiation after atmospheric attenuation (noted as I in Fig. 6), whereas the NARR estimates of direct beam irradiance $B \downarrow$ at the surface already account for the solar illumination angle on the basis of the NARR terrain. The topographic adjustment consists of multiplying $B \downarrow$ by the scaled cosine of solar illumination angle $\cos \theta^S$ defined as the ratio of the cosine of solar illumination angle on the 1 km DEM to that on the NARR terrain as illustrated in Fig. 6.

To perform the topographic correction, the cloudiness corrected NARR hourly total incoming shortwave radiation is partitioned into direct beam irradiance $B \downarrow(i,j)$ and diffuse irradiance $F \downarrow(i,j)$ using the shortwave atmospheric transmittance. Diffuse and direct radiation fluxes are affected by the terrain in different ways. The upwelling reflected radiation from the surrounding terrain $F \uparrow(i,j)$ is estimated as follows

$$F \uparrow(i,j) = r(i,j)[F \downarrow(i,j)(1 - V_d(i,j)) + \cos \theta_0 B \downarrow(i,j)] \quad (10)$$

where $r(i,j)$ is the surface reflectance (albedo). The sky view and terrain configuration factors, respectively V_d and C_t , are calculated using the Image Processing Workbench software (IPW) (Frew, 1990) based on high-resolution elevation data (see Fig. 7 for V_d and C_t in the IPHEX domain). The original methodology can be found in Dubayah and Paul (1995) and Dubayah and Loeschel (1997).

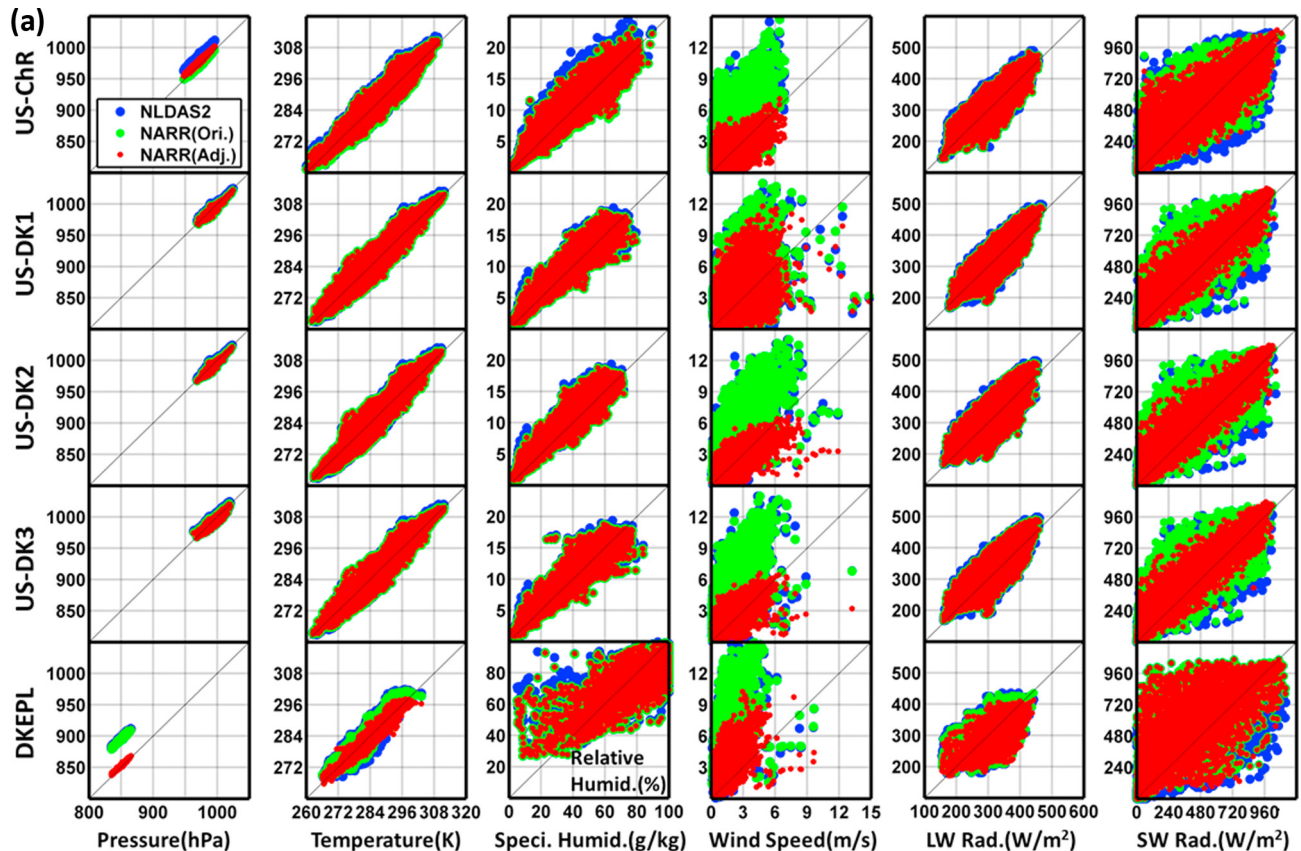


Fig. 10. (a) Comparison between observed (x-axis) and estimated (y-axis) atmospheric pressure, atmospheric temperature, atmospheric specific humidity, wind speed, downward longwave radiation and shortwave radiation from NLDAS2, NARR before (Ori.) and after (Adj.) elevation correction in the five year period, at four Ameriflux towers, namely US-CHR, US-Dk1, US-Dk2, US-Dk3, and the DKEPL tower from the top to the bottom, respectively. Due to lack of observations, estimates of relative humidity (%) at DKEPL are used instead of specific humidity. Time series of air temperature, atmospheric pressure and wind speed at US-CHR (b) and DKEPL (c) 2007–2011. Shaded regions indicate that quality observations are available.

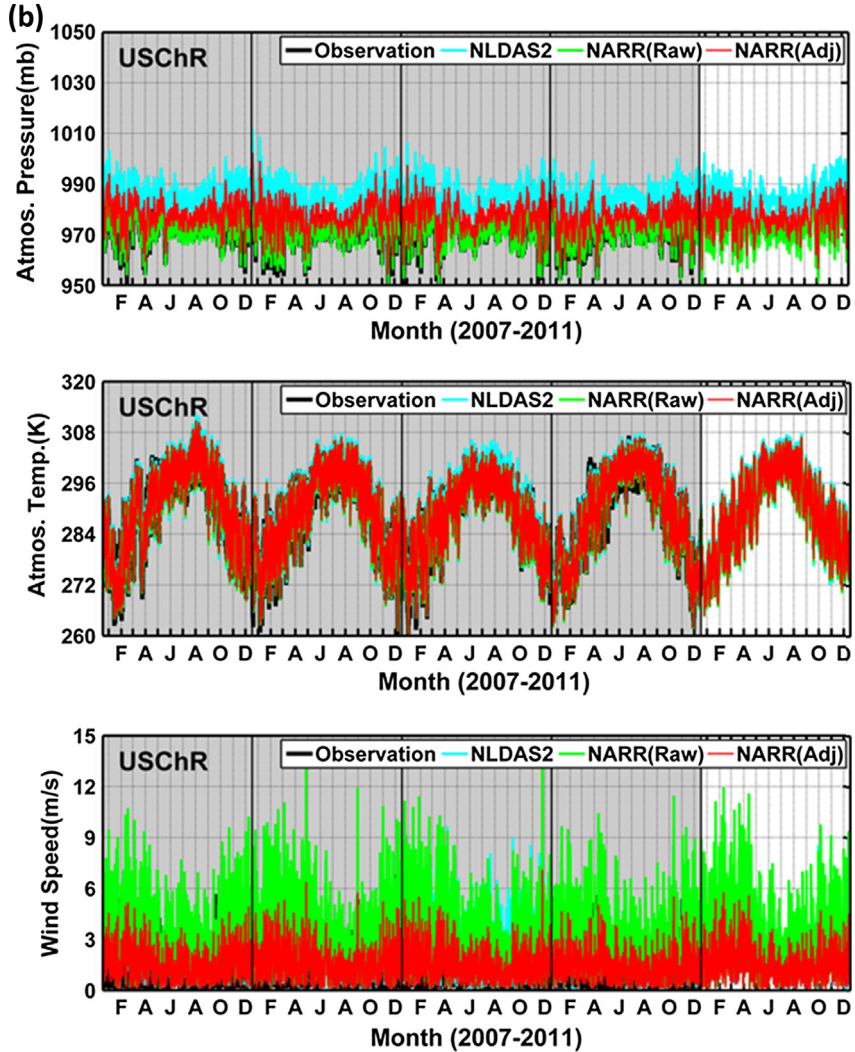


Fig. 10 (continued)

The sky view factor V_d is given by:

$$V_d = \frac{1}{2\pi} \int_0^{2\pi} [\cos S \sin^2 H_\phi + \sin S \cos(\phi - A) \times (H_\phi - \sin H_\phi \times \cos H_\phi)] d\phi \quad (11)$$

where S and A are slope magnitude and aspect, and H_ϕ is the zenith angle with regard to the local horizon in view direction ϕ . For simplicity, the location (pixel) subscripts (i,j) are not used in Eq. (11), but all relevant variables are calculated on a pixel basis. In open areas, the sky view factor V_d is large, but is small at the bottom of narrow valleys where the sky is partially obstructed (Fig. 7, left panel).

The terrain configuration factor $C_t(i,j)$ estimates the fraction of the surrounding terrain that is visible from location (i,j) and varies from 0 (only sky visible) to 1 (only terrain visible):

$$C_t \approx \frac{1 + \cos S}{2} - V_d \quad (12)$$

Thus, the product $C_t(i,j)F \uparrow(i,j)$ is the radiation received at point (i,j) that is reflected by the surrounding visible terrain. Generally, the smaller the terrain configuration factor C_t , the larger the sky view factor V_d (Fig. 7).

3. Results and evaluation

The downscaled atmospheric forcing datasets were evaluated against available flux tower observations (Table 2) in the SE US, and compared against the NLDAS-2 primary forcing data at the same location for reference. The objective is twofold: (1) to show that the downscaling and corrections applied do introduce physically-based improvements in regions of complex topography that are not represented at NARR resolution, and (2) to show that the downscaling methodology improves, or it does not degrade, the NARR fields elsewhere away from the mountains. The spatial scale of flux tower observations varies in time and depends highly on the height and location of the tower, land-form, land-use class and land-cover heterogeneity surrounding the towers, and regional weather conditions that determine Lagrangian transport and mixing. Thus, the multi-year tower observations are used to evaluate the model's ability to capture the local hydrometeorological regime in the statistical mean sense. The number of flux-towers in complex terrain is small (US-ChR, US-WBW, and DKEPL, Table 2), and only DKEPL is located at high elevation in the SAM.

3.1. Elevation correction and wind adjustment

Selected results of the adjusted (downscaled and corrected) and the original NARR atmospheric pressure and temperature (Fig. 8),

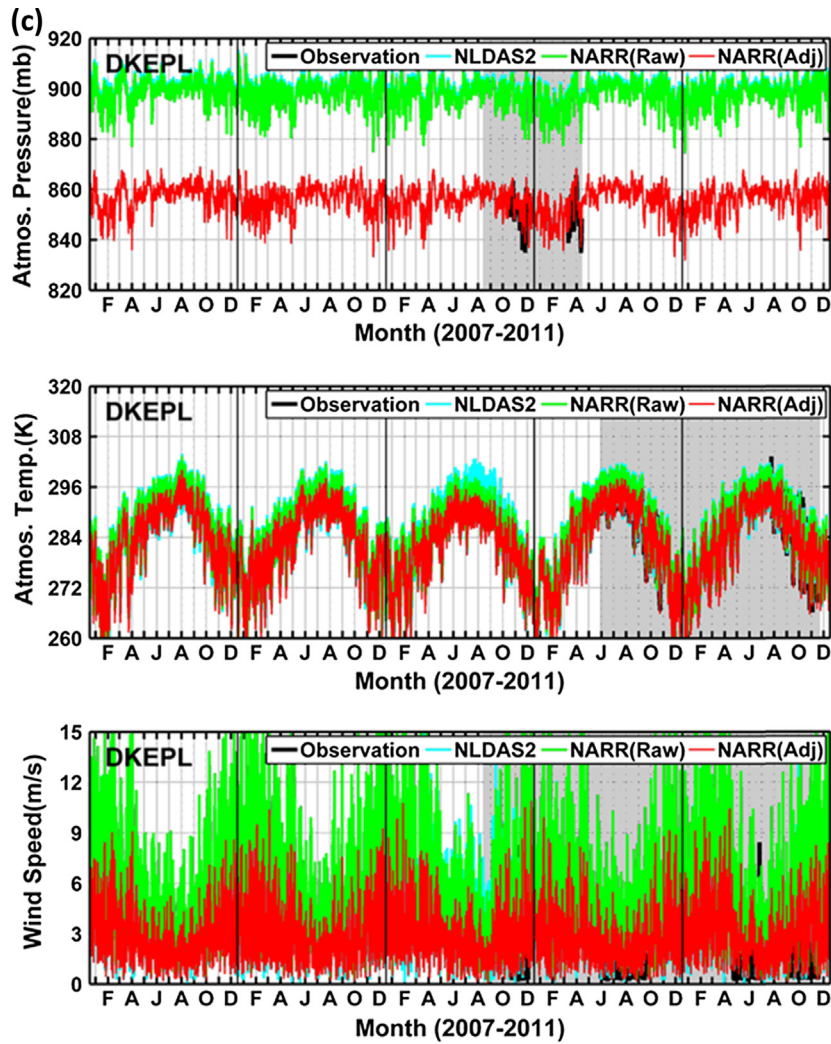


Fig. 10 (continued)

Table 3

Summary of RMSEs for the various products at the tower locations. The best performance/lowest RMSEs are bolded. Note that due to the lack of direct observations, relative humidity is used instead of specific humidity.

| Tower | Data | Air Temp. (K) | Air Pressure (hPa) | Specific Humidity (g/kg) | Wind Speed (m/s) | Longwave Radiation (W/m ²) | Shortwave radiation (W/m ²) |
|--------|------------|---------------|--------------------|--------------------------|------------------|--|---|
| US-ChR | NLDAS2 | 2.45 | 13.14 | 1.55 | 2.14 | 26.28 | 103.26 |
| | NARR (Ori) | 2.21 | 1.21 | 1.29 | 2.18 | 24.73 | 100.28 |
| | NARR (Adj) | 2.15 | 5.04 | 1.28 | 0.85 | 24.68 | 75.19 |
| US-Dk1 | NLDAS2 | 2.47 | 1.64 | 1.33 | 2.33 | 25.60 | 82.66 |
| | NARR (Ori) | 2.64 | 4.05 | 1.23 | 2.36 | 25.31 | 100.02 |
| | NARR (Adj) | 2.64 | 4.04 | 1.23 | 1.98 | 25.31 | 71.60 |
| US-Dk2 | NLDAS2 | 2.38 | 1.26 | 1.55 | 2.36 | 33.12 | 82.42 |
| | NARR (Ori) | 2.33 | 2.95 | 1.35 | 2.40 | 32.72 | 103.31 |
| | NARR (Adj) | 2.32 | 3.46 | 1.34 | 0.88 | 32.65 | 75.13 |
| US-Dk3 | NLDAS2 | 2.42 | 3.16 | 1.37 | 2.72 | 31.38 | 81.49 |
| | NARR (Ori) | 2.52 | 2.49 | 1.29 | 2.76 | 30.87 | 100.43 |
| | NARR (Adj) | 2.50 | 3.01 | 1.28 | 0.93 | 30.71 | 71.94 |
| DKEPL | NLDAS2 | 2.84 | 46.16 | 12.95% (RH) | 4.17 | 44.24 | 139.50 |
| | NARR (Ori) | 2.50 | 44.71 | 12.15% (RH) | 4.22 | 43.47 | 163.64 |
| | NARR (Adj) | 1.54 | 2.78 | 12.12% (RH) | 1.85 | 44.22 | 156.45 |

and wind speed (Fig. 9) are used here to examine spatial variability with a focus on the diurnal cycle. The specific humidity and downward longwave radiation data exhibit similar behavior, and are not shown here. One should be mindful of the differences in spatial

scales among the various products: 32 km for NARR, 12.5 km for NLDAS-2, and 1 km for the downscaled IPHEx data.

The adjusted fields in Figs. 8 and 9 vary over a wide range of magnitude compared with the original fields in regions of complex

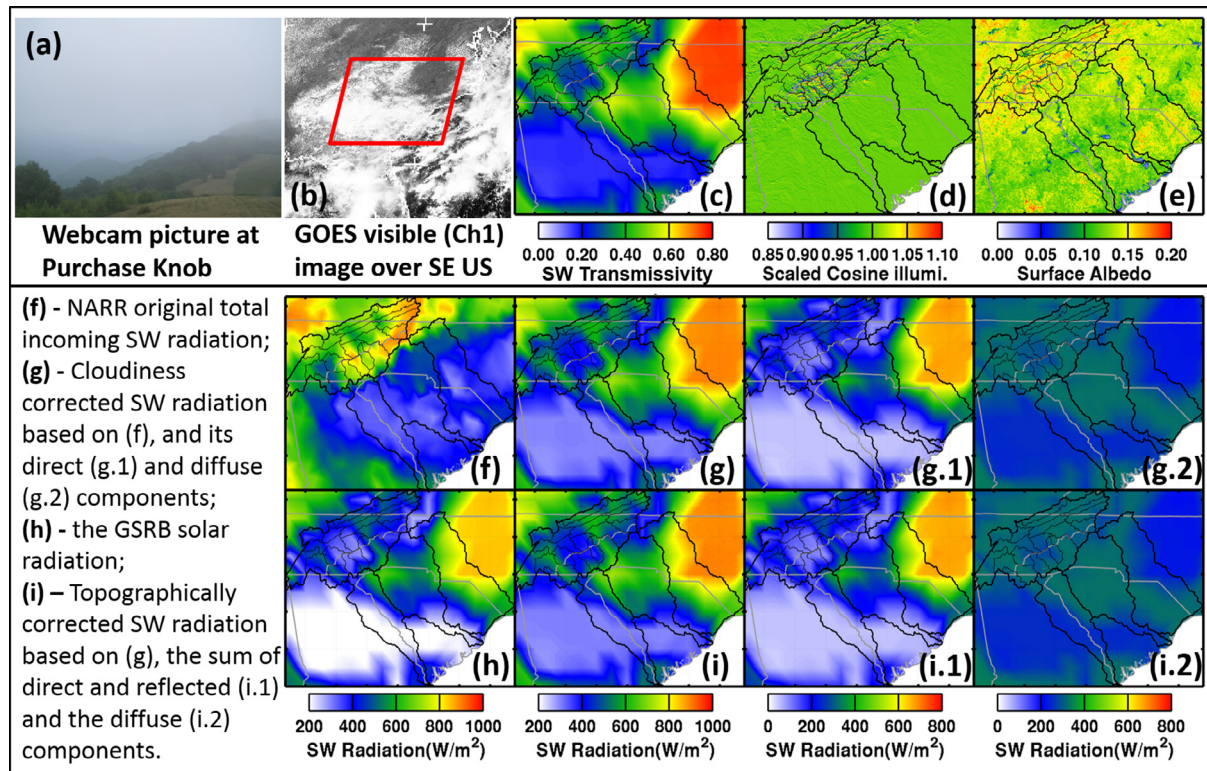


Fig. 11. An example showing the intermediate steps in the application of cloudiness and topographical corrections to the NARR original total incoming shortwave radiation over the SE US at 1 PM (EST) on Sep. 1, 2009. Cloudy conditions are shown by (a) an archived picture (http://www2.nature.nps.gov/air/webcams/parks/grsmplcam/grsmpl_arccfm) from a webcam (looking northeast) installed at Purchase Knob (very close to the DKEPL tower as indicated in Fig. 1), and (b) a GOES visible (Channel 1) image of the cloudiness pattern covering the whole SE US with a red parallelogram indicating the IPHEx domain. The time-variant auxiliary input parameters for the correction, including the derived SW transmittance, the scaled cosine of the local illumination angle, and surface albedo are shown in (c), (d) and (e), respectively. Panel (f) is the NARR original total incoming shortwave radiation, and (g) is the NARR radiation after cloudiness correction which consists of the direct (g.1) and diffuse (g.2) components partitioned by the transmittance (c). Panel (h) depicts the GCIP SRB (GSRB) solar radiation product used here as reference. Panel (i) shows the final corrected incoming shortwave radiation with cloudiness and topographical correction, and its two components (i.1), and the diffuse component (i.2).

terrain, specifically in the Appalachian Plateaus and the Blue Ridge, including the Pigeon River Basin (Fig. 1c). The largest variability in the adjusted NARR fields is in atmospheric pressure with strong contrasts between ridges and valleys as expected (Fig. 8, left panel). Note that NLDAS-2 forcing fields were corrected for the elevation effects based on NLDAS topography, which is quite coarse for this region. Generally, the adjustments of atmospheric pressure and near-surface air temperature, specific humidity, and downward longwave radiation are much smaller along ridge lines than in the valleys, and exhibit strong temporal variability at seasonal and diurnal scales (not shown). For example, the differences between adjusted atmospheric temperature and the original NARR values are much larger in the winter than in the summer (Fig. 8, bottom right panel).

Fig. 9 shows spatial wind fields at different hours of the day on March 1, 2009. Unlike other atmospheric forcing fields, the spatial variability in wind speed depends primarily on surface roughness length and displacement height parameters, which are specified according to land-cover type, and not on topography explicitly because the physical parameterization used here cannot explicitly resolve mesoscale circulations in complex terrain below the NARR nominal resolution as pointed out in Section 2.3. Although the adjusted friction velocity shows larger values than the original friction velocity (not shown), the downscaled wind speed is systematically lower than the original NARR due to the impact of increased spatial resolution on the specification of displacement height based on land-cover class (e.g. large blue areas in the bottom row in Fig. 9). The largest difference between the friction velocity and wind speed before and after adjustment is in urban areas, where the effective roughness length is large (about 2.5 m). The

flux tower observations from the AmeriFlux network and the Duke tower in the Southern Appalachians (marked in Fig. 1c) are used next for independent evaluation at local (point) scales.

Scatter plots of original NARR, adjusted NARR as well as NLDAS-2 data against the tower observations are presented in Fig. 10a, and the associated Root Mean Squared Errors (RMSEs) are summarized in Table 3. Overall, the adjusted NARR fields show better agreement, or at least as good as the original NARR, though NLDAS-2 outperforms NARR with or without adjustment at times in the case of air temperature at low elevations. Note that the three towers in Duke Forest (US-Dk1, US-Dk2, US-Dk3, see Fig. 1c) are very close together though in fields with distinct land-cover, and thus RMSE differences can be interpreted as a measure indicative of spatial uncertainty. The RMSE of the adjusted atmospheric pressure at DKEPL is reduced from 44.71 hPa to 2.78 hPa, with small surface pressure differences for other towers because of the small elevation differences in the Piedmont and elsewhere away from complex topography (Fig. 1c and Table 2). Time-series of surface pressure, air temperature, and wind speed at US-ChR (Fig. 10b) and DKEPL (Fig. 10c) illustrate the robustness of the NARR adjustments from daily to inter-annual scales over the period 2007–2011. The downscaled specific humidity and wind speed outperform other estimates (i.e. the original NARR and NLDAS-2) at all towers at all times. Despite limitations pointed out earlier, the proposed wind scaling relationship works well at the mesoscales tested here. This is an important result with far reaching implications for the calculation of surface heat fluxes, and especially evapotranspiration rates.

The adjusted radiation fluxes show improvement at all AmeriFlux towers. Cloud and topographic corrections applied to incoming shortwave radiation result in significant improvements with

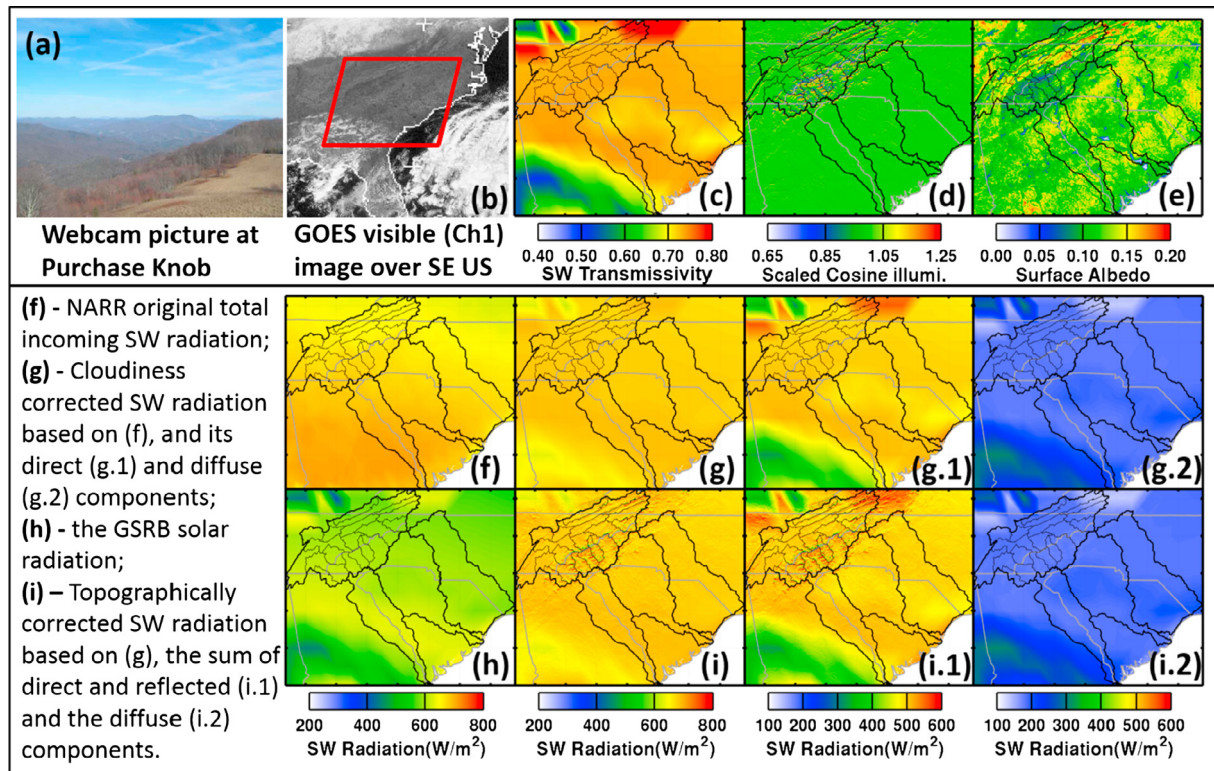


Fig. 12. Same as Fig. 11 for a clear-sky conditions at 1 PM on Feb. 1, 2009.

large RMSE decreases of 25–30 W/m² at low elevation towers, and about 1/3 of this value at DKEPL (Table 3). These results are explored in further detail next.

3.2. Topographic and cloudiness correction of shortwave radiation

The cloudiness and topographic corrections were dynamically applied to the regional radiation at hourly scale with aid of time-invariant auxiliary parameters (shortwave transmittance, surface albedo, and the cosine of the local illumination angle) as described in Section 2.4.

Figs. 11 and 12 show the intermediate results after performing the cloudiness and topographic correction for cloudy and clear-sky conditions, respectively. The clear-sky and cloudy/foggy conditions were confirmed by review of archived webcam pictures (panel 11.a). In Fig. 11, both the GSRB solar radiation (panel 11.h) and the derived atmospheric transmissivity (panel 11.c) vary strongly with cloud cover (see the corresponding GOES visible image in panel 11.b), but the cloud pattern in the original NARR (panel 11.f) must be corrected (panel 11.g). Panel (11.i) in Fig. 11 shows the final radiation results after both cloudiness and topographic corrections. Note the very good agreement with the GSRB data and GOES imagery with regard to the cloudiness patterns. In Fig. 12, the GSRB radiation data and the transmissivity exhibit uniform distributions, except for the cloud band in the southwest corner (green bands in panels 12.c and 12.h). The cosine of the solar illumination angle mainly affects the direct radiation component. Thus, in cloudy conditions, the direct radiation component is very small, especially in the mountains where the illumination effects are large (panels 11g.1 and 11i.1), and the topographic effects are not apparent in the final radiation estimates. In other words, the cloudiness correction dominates over the topographic correction for cloudy and partially cloudy conditions. By contrast, for clear-sky conditions, the topographic effects are apparent in the mountains, displaying complex spatial variability in the Southern Appalachians as shown in

panel (12i.1), and thus the topographic corrections dominate the spatial variability in the total shortwave radiation. The final corrected radiation shows the effect of the small band of clouds in the southwest corner, while capturing realistic topographic variability.

The diurnal and seasonal cycles of downscaled and corrected NARR shortwave radiation, as well as the original NARR and NLDAS2 shortwave radiation are shown in Fig. 13. At a particular time, the difference between the shortwave radiation before and after corrections can be as large as ~500 W/m² (e.g. the example shown for a day in June). The topographic effects are apparent in winter, especially in the early morning or late afternoon, in the Blue Ridge and Appalachian Plateaus regions (Fig. 1c, Fig. 13), but the cloudiness correction is dominant overall. For instance, there is partial cloud cover in the SE US at noon on Dec. 15 in 2009 in both the NLDAS2 and original NARR downward shortwave radiation. However, the GOES visible imagery³ displays uniform cloud coverage (i.e. 100% thick cloud cover). After correction, the adjusted NARR shortwave radiation field consists of uniformly lower values compared to the original data, as it should.

Generally, both the original NARR and NLDAS-2 fields overestimate the incoming shortwave radiation compared to the tower observations (Fig. 10). The adjusted NARR shortwave shows the best agreement with the tower observations everywhere (Table 3) except at DKEPL. This can be attributed in part to the fact that the GSRB product was discontinued in mid-2010, whereas the tower observations are only available from 2009 onwards, and thus the period of higher quality cloud corrections is very short. In addition, the notional physical scale-gap at high-elevations in complex topography is very large due to unresolved mesoscale processes in NARR. The original and adjusted radiation represent average values of otherwise heterogeneous fields over significantly different

³ The image at noon is missing, but the images at 1500 and 2100 UTC are available from: <http://www.sat.dundee.ac.uk/geobrowse/>.

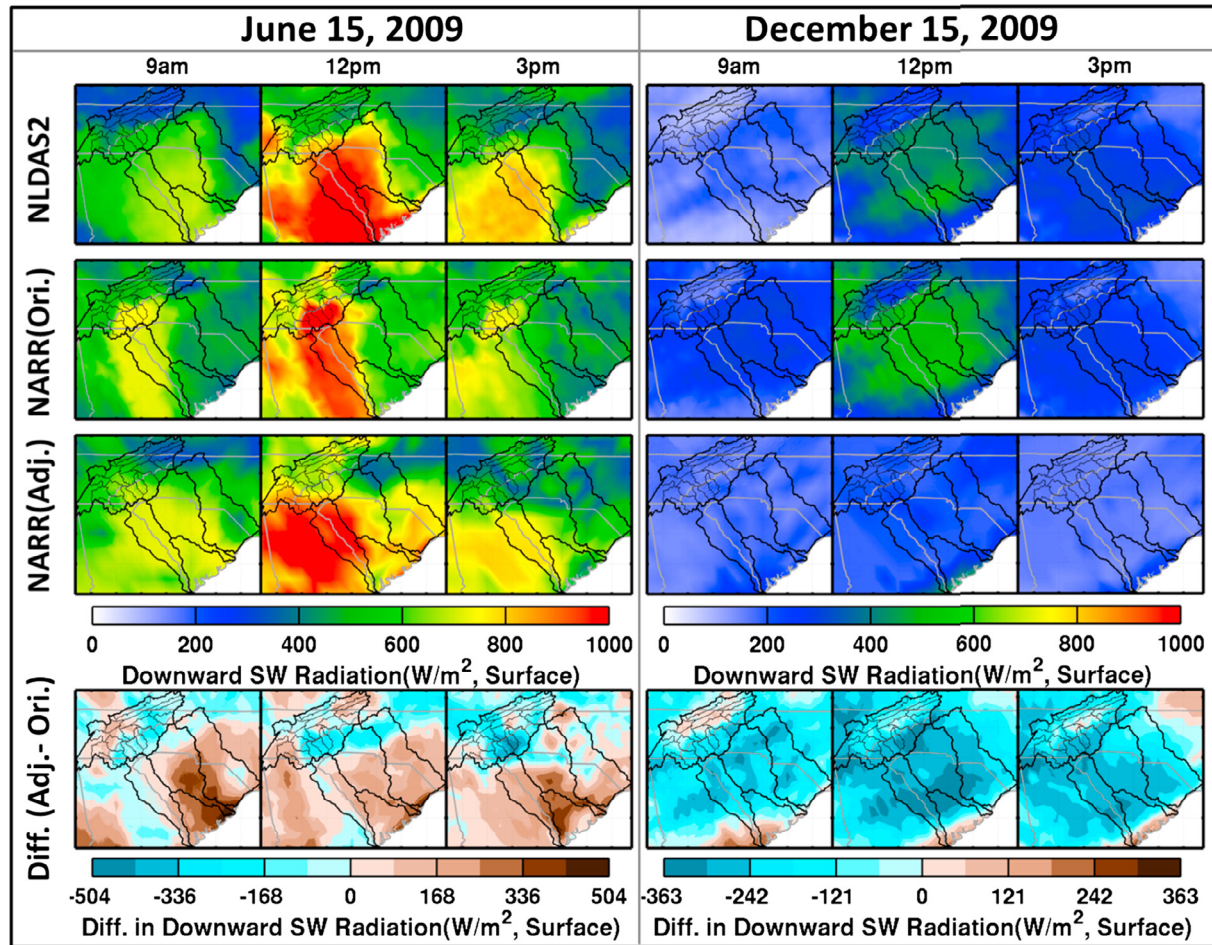


Fig. 13. Downward shortwave radiation at the surface over the SE US from NLDAS2, NARR before (Ori.) and after (Adj.) cloudiness and topographic correction at 9 AM, noon and 3 PM (EST) on Jun. 15 and Dec. 15 in 2009. The bottom panels show the difference between the NARR downward shortwave radiation after and before corrections, using a symmetrical blue-brown color scale such that the brown color represents positive values and the blue color represents negative values.

areas ($\sim 1000 \text{ km}^2$ and 1 km^2 respectively), and thus discrepancies with regard to the tower observations (point to field scale) are expected. This artifact is further enhanced by the persistence of small-scale low level fog and clouds that are not detected from satellite. At mid-day in winter, when fog is present at DKEPL (e.g. Wilson and Barros, 2014), the NARR based estimates consistently overestimate shortwave radiation.

4. Water and energy budget impacts – hydrologic modeling application

The utility of the downscaled atmospheric forcing datasets for hydrological applications is demonstrated for 4 continuous water-year simulations (2007 Oct. to 2011 Sep.) in the Pigeon River Basin (PRB, area $\sim 1823 \text{ km}^2$, Fig. 1c), a tributary of the Upper Tennessee River Basin, using the spatially distributed Duke Coupled surface-groundwater Hydrology Model (DCHM, formerly 3D-LSHM; Tao et al. 2016; Tao and Barros, 2014a; Tao and Barros, 2013; Yildiz and Barros, 2007). For reference, the area of the PRB is smaller than two NARR grid elements (each 1024 km^2), and there are two thousand grid elements in the DCHM grid for the PRB (larger area than actual basin area to accommodate complex outer boundary).

The lack of radar observations and long-term raingauges impairs the quality of the rainfall products, downscaled or not, in the inner region of the SAM (e.g. Tao et al., 2016; Nogueira and Barros, 2015).

Instead of NARR rainfall, the National Stage-IV⁴ Quantitative Precipitation Estimates (QPE) combining radar and raingauge observations are used instead. The Stage-IV QPE data (available at 4 km resolution) were down-scaled to 1 km resolution via bilinear interpolation (Stage-IV-Bi) and using a transient multifractal ensemble approach (Stage-IV-TF) as described by Nogueira and Barros (2015). The Stage-IV-Bi rainfall product is used for the simulations with the bi-linearly interpolated original NARR atmospheric forcing products, and the Stage-IV-TF rainfall product is used with the corrected down-scaled NARR products (Nogueira and Barros, 2014a).

4.1. Hydrologic model implementation

The DCHM implementation used in this study is similar to Tao et al. (2016). Soil properties and other hydrologic parameters are the same as in Tao and Barros (2013, 2014a and 2014b), and landscape attributes including radiative properties and land-use and land-cover were specified according to Tao and Barros (2014b), and all are available from <http://iphex.pratt.duke.edu>. For sensitivity analysis, the DCHM was driven separately by the original and the corrected down-scaled atmospheric forcing from NARR and hourly precipitation from the IPHEx2014 data sets as described above. Back-to-back “spin-up like” simulations consisting of repeated 4-year simulations using the same atmospheric forcing

⁴ <http://www.emc.ncep.noaa.gov/mmb/ylin/pccpanl/stage4/>.

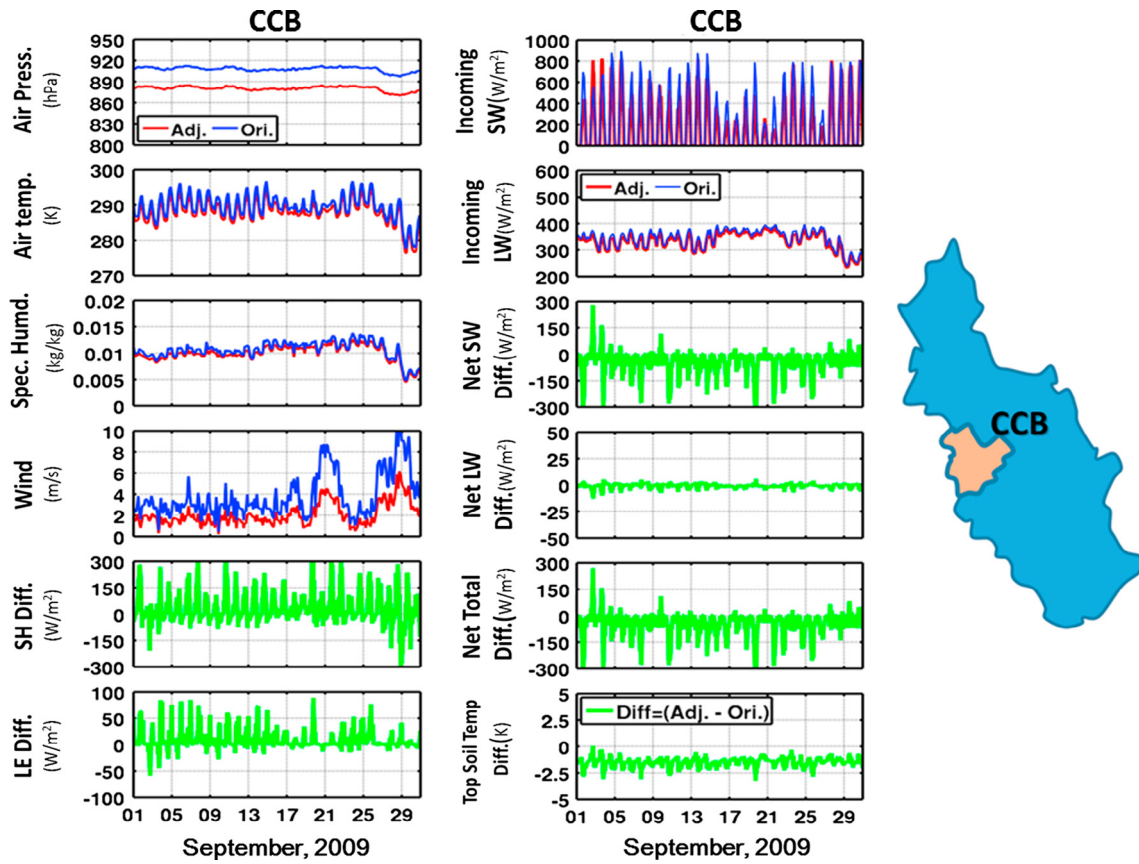


Fig. 14. Areal averages over the Cataloochee Creek Basin (CCB) within the Pigeon River Basin (PRB) during September 2009. Left: Time series of air pressure, air temperature, specific humidity, and wind velocity. Differences in sensible heat flux (SH Diff.) and latent heat flux (LE Diff.) simulated by the model using original downscaled NARR forcing and adjusted forcing are shown in the two bottom rows. Center: Time series of incoming shortwave and longwave radiation. The difference in net shortwave radiation (Net SW Diff.), net longwave radiation (Net LW Diff.), net total radiation (Net Total Diff.) and top soil temperature (Top Soil Temp Diff.) between model simulations using original downscaled NARR forcing and adjusted forcing are shown in the lower four rows. Right: Schematic location of CCB within the PRB. Blue lines correspond to original downscaled NARR data without adjustment. Red lines indicate data with adjustment. Green lines are differences between model simulations forced with adjusted and original downscaled NARR forcing. (For interpretation of the references to color in this figure legend, the reader is referred to the web version of this article.)

and initial soil moisture and water table conditions equal to the values at the end of the preceding 4-year iteration were conducted until differences between two successive 4-year streamflow simulations were less than 1% over the 4-year simulation period up to ten repetitions, or 40 years.

The performance of the uncalibrated DCHM was evaluated for several small basins within the PRB (Tao et al., 2016; Tao and Barros, 2014b) including the Cataloochee Creek Basin (CCB, area $\sim 127 \text{ km}^2$) that is used here for illustrative purposes as representative of headwater catchments in the SAM (Tao and Barros, 2013, 2014a and 2014b). The CCB (delineated in Fig. 14, right panel) is nestled in the inner region of the Southern Appalachian Mountains (SAM) spanning 1127 m of elevation difference, and it is one of only 50 watersheds in the United States Geological Survey (USGS) national Hydrologic Benchmark Network (Mast and Turk, 1999). Improvements in the DCHM simulations for the PRB, and the CCB in particular, reflect the benefit of using the adjusted downscaled atmospheric forcing including the Stage-IV-TF rainfall.

4.2. Sensitivity analysis

The Nash-Sutcliffe Efficiency (NSE)⁵ metric applied to river discharge at hourly time-scale and integrated over the four year period

of simulation doubled for the CCB using the adjusted downscaled data sets (Tao and Barros, 2014b), but this large improvement in streamflow reflects in great part the improvements in the rainfall between Stage-IV-Bi and Stage-IV-TF as discussed by Nogueira and Barros (2014a and 2015). Where the Stage-IV product is of higher quality across the PRB (i.e. eastern and western slopes of the SAM at low elevations), the NSE increases are in the 10–30% range (Tao and Barros, 2014b; Nogueira and Barros, 2014a, 2015), which is nevertheless a large improvement in hydrologic modeling performance skill without calibration, especially considering the hourly temporal resolution and the multi-year simulations. The higher NSE scores encompassing both response to large storms and periods of low flows, and therefore they also reflect improvements in simulated soil moisture in response to improved rainfall forcing in the PRB (e.g. Tao and Barros, 2013).

Area-averaged hourly surface energy flux differences between DCHM simulations using the adjusted and the original NARR atmospheric forcing during September of 2009⁶ are shown in Fig. 14 for the CCB. The CCB NSE improved from 0.21 to 0.48 for this month, but by less than 5% in PRB sub-catchments where the quality of original rainfall products is good ($\text{NSE} > 0.7$; Tao and Barros, 2014b). The relevant forcing fields including air pressure, air temperature, specific humidity and wind velocity are shown in the left column (Fig. 14, top four rows). Differences in surface pressure (up to 35 hPa) and

⁵ $NSE = 1 - \left[\sum_{t=1}^N (Q_o^t - Q_m^t)^2 / \sum_1^N (Q_o^t - Q_o^{mean})^2 \right]$, where Q_o and Q_m are respectively the observed and simulated streamflow, and $N = 4 \text{ years} \times 365 \text{ days} \times 24 \text{ h}$.

⁶ NB: This month is selected to follow discussion regarding shortwave radiation adjustments, Section 3.2, Fig. 11.

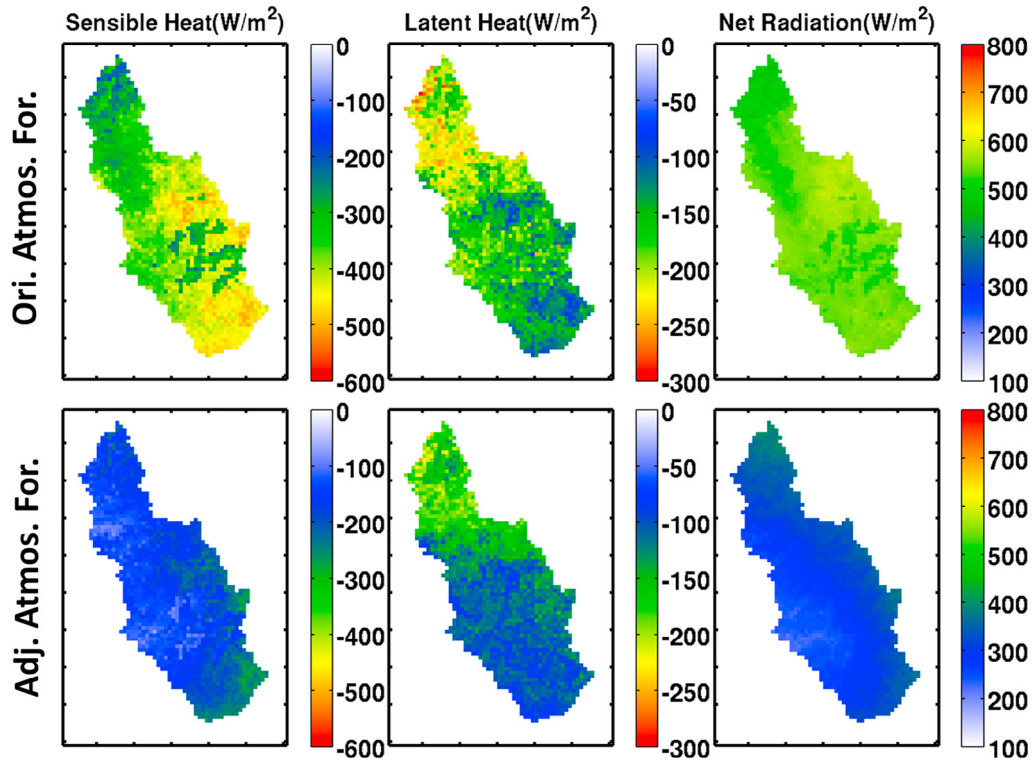


Fig. 15. Spatial distribution of simulated sensible heat, latent heat and net radiation using original atmospheric forcing fields before (top) and after the adjustment (bottom), for cloudy conditions (1 PM on Sep. 1, 2009) over the Pigeon River Basin.

air temperature (up to 5 K) reflect the difference between the DCHM topography and the NARR terrain in the CCB. The changes are small for specific humidity since these data are essentially interpolated bilinearly from the original NARR fields without further correction. By contrast, the differences in near-surface wind are very large and vary widely from day to day depending on synoptic conditions. Negative signs in the model energy fluxes indicate that the flux is leaving the land surface to the atmosphere (i.e. upward fluxes). Thus, negative differences (Adj. - Ori.) mean that the absolute magnitude of energy fluxes using the adjusted downscaled forcing is larger than using the original NARR forcing fields (two bottom rows). Generally, the absolute magnitudes of both sensible and latent heat fluxes are larger using original fields with positive differences (i.e. bias) mostly during daytime up to 300 W/m^2 and 100 W/m^2 for sensible and latent heat fluxes, respectively (Fig. 14, left column, bottom two rows).

Interestingly, days with large differences in surface winds do not necessarily correspond to the days with the largest differences in surface fluxes (Fig. 14, left). For weak and moderate wind conditions in the first two weeks of September 2009, inspection of the radiative fluxes (Fig. 14, center) reveals that the primary forcing behind day-to-day variations in the surface energy fluxes is the incoming shortwave radiation. When the winds pick-up in the second half of the month due to changes in synoptic weather conditions, there is a strong impact on sensible heat fluxes ($\pm 300 \text{ Wm}^{-2}$) even as the changes in shortwave radiation are modest ($< 50 \text{ Wm}^{-2}$). Further, despite complex topography, the area averaged radiation fluxes are very similar (not shown) from one PRB sub-catchment to another at high elevations in the inner SAM. Ridgeline clouds strongly affect the diurnal cycle of incoming shortwave radiation (Wilson and Barros, 2014, 2015), which are not resolved in the original NARR data, and thus the adjusted incoming shortwave radiation fluxes using GSRB data are lower than the original values, except for two clear days (Sep. 2 and 3). The net radiation calculated from the original radiation forcing (as shown in the 5th row in 5, central column), results in larger

temperature increases in the top soil layer (6th row), which in turn affects the sensible heat flux as shown in the left column (5th row) as well as the latent heat flux (bottom row) depending on soil moisture conditions (large latent heat flux differences on September 19 contrasting with very small differences on September 21).

Spatial distributions of simulated sensible heat flux, latent heat flux and net radiation fields using original atmospheric forcing and the adjusted NARR fields are shown at mid-day across the PRB for cloudy and clear-sky conditions in Figs. 15 and 16, respectively. For the cloudy scenario on Sep. 1 (previously discussed in Section 3.2, Fig. 11), cloud covers most of the basin, and thus the adjusted incoming solar radiation is much lower than the original NARR values (up to -331 W/m^2 on average) leading to large discrepancies in sensible heat flux (up to 297 W/m^2). For the clear-sky scenario on Sep. 2, the total net radiation flux (net shortwave plus net longwave) exhibits wide spatial variability with large values at high elevations and relatively low values at low elevations as expected (Fig. 16). Latent heat fluxes display strong spatial organization with clearly demarcation of high elevation areas with shallow soils, where evapotranspiration is limited by soil moisture, and low elevation areas with deep soils. Stronger gradients under cloudy conditions (Fig. 15) are consistent with larger differences in surface temperature. This sensitivity analysis highlights the importance of accurate estimates of incoming solar radiation and net radiation in mountainous regions where foggy and cloudy conditions are persistent features that can introduce large differences in surface fluxes (e.g. Wilson and Barros, 2015). This is essential to capture the spatial variability of microclimates and complex eco-hydrology in the SAM, and elsewhere.

5. Summary and discussion

High resolution (1 km, hourly) atmospheric forcing datasets including 10 m ABG air temperature, air pressure, wind velocity,

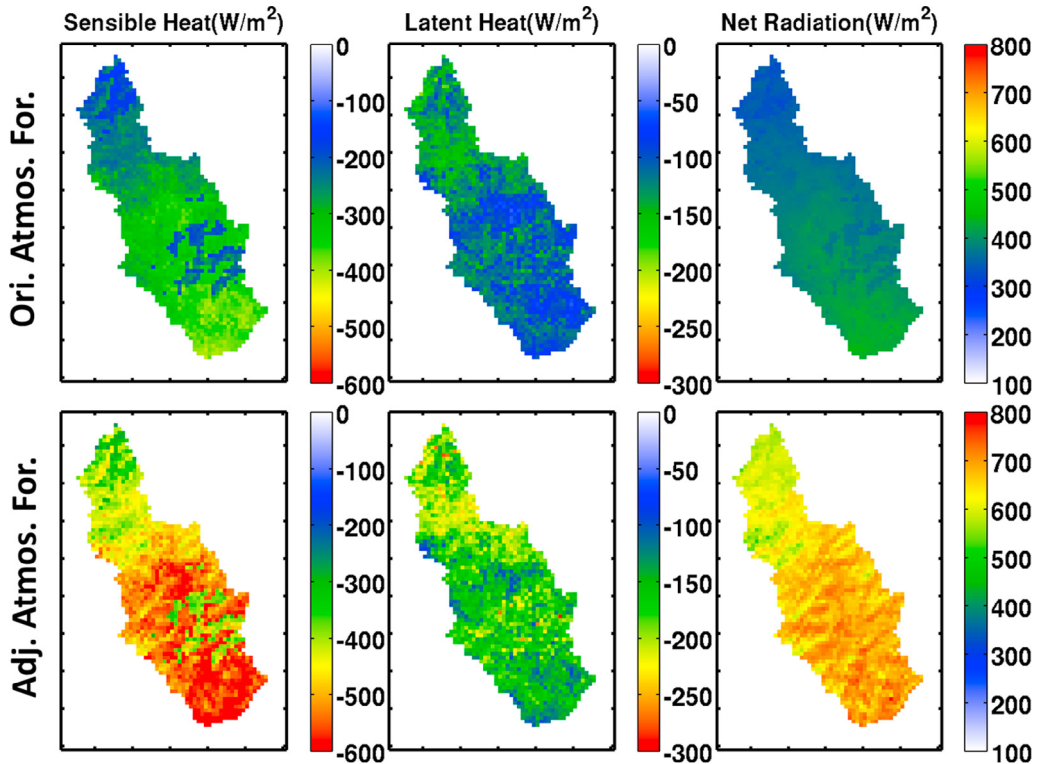


Fig. 16. Spatial distribution of simulated sensible heat, latent heat and net radiation using original atmospheric forcing fields before (top) and after the adjustment (bottom), for clear-sky conditions (1 PM on Sep. 2, 2009) over the Pigeon River Basin.

specific humidity, downward shortwave and longwave radiation were developed for the IPHEx2014 domain based on the NARR products originally at 32 km spatial resolution and 3-h temporal resolution, for a seven-year period (2007–2013) over the Southeast US (see Table 1 for data access information). The elevation correction was applied to the NARR air temperature, air pressure, specific humidity and downward longwave radiation, and dynamic lapse rates were derived from the estimated atmospheric temperature profiles. Friction velocity was adjusted based on a relationship between the geostrophic drag coefficients and the Rossby number, which was used subsequently to estimate wind velocity at high spatial resolution. Downward shortwave radiation data were first interpolated to hourly time intervals using a temporal interpolation method based on the solar zenith angle as well as the diurnal cycle of NARR cloudiness. Real-time cloudiness patterns derived from the GSRB dataset were used to correct cloudy effects for NARR shortwave radiation by matching the spatial PDF of NARR data to that of the GSRB data, and topographic effects were incorporated based on a well-established topographic solar radiation model. Nevertheless, unquantified uncertainty in the cloud corrections is expected at different times and locations due to the lack of high-resolution observations generally, as well as well-documented weaknesses in the simulation of clouds in atmospheric models (e.g. Wilson and Barros, 2015).

A comprehensive evaluation of the adjusted downscaled NARR products would require a dense network of ground-based measurements to capture the spatial and temporal variability of cloud cover, water and energy fluxes in complex terrain. Because such observing system does not exist, the evaluation scope is therefore limited to existing observations, and we take advantage of long records to demonstrate robust long-term behavior. Sensitivity analysis of long duration hydrologic simulations was used to

examine the impact of atmospheric forcing on the various terms of the surface water and energy budget equations, which are nonlinearly related.

Overall, as expected, the adjusted downscaled atmospheric forcing datasets exhibit larger spatial variability compared to the original NARR fields consistent with the 1:32 spatial scale ratio. The comparison among the atmospheric forcing data and flux tower observations in the region (AmeriFlux and DKEPL) reveals that the adjustments to the NARR fields result in improvements on the order of 50–100% for near-surface winds everywhere, 10's hPa for surface pressure as well as large differences in air temperature (up to 6 K) at high elevations. A decrease of 25–30 W/m² in the RSMEs of shortwave radiation estimates at low-elevation flux-towers amounts to approximately 10% of monthly net radiation in the warm season, and thus is a very significant contribution toward reducing the uncertainty in the surface energy budget. Further, simulations with a fully-distributed, coupled surface-groundwater hydrologic model (DCHM) using both the original and adjusted downscaled atmospheric forcing from NARR exhibit large sensitivity to atmospheric forcing of various terms in the surface water and energy budgets with differences in peak latent, sensible and net radiation fluxes of 100's of W/m² at mid-day in the warm season. Concurrent changes in air temperature, incoming shortwave radiation and wind speed impact nonlinearly sensible heat fluxes and latent heat fluxes [3:1 ratio] with the latter being constrained by soil moisture controls of evapotranspiration, especially at high elevations. Though hydrologic sensitivity will vary from one location to another depending on regional climate and physiography, these results highlight the importance of atmospheric forcing in hydrologic predictability, and therefore the need for appropriate downscaling and correction methods to derive realistic atmospheric forcing fields.

Acknowledgments

This work was supported by NASA's Precipitation Measurement Missions and GPM Ground Validation Program under grants (NNX13AH39G and NNX14AE71G). We are grateful to Dr. Rachel Pinker and Dr. Chuan Li for their help with the GCIP SRB data, and to Lauren Lowman and two anonymous Reviewers for constructive review comments that improved the manuscript.

References

- Barros, A.P., et al., 2014. NASA GPM-Ground Validation: Integrated Precipitation and Hydrology Experiment 2014 Science Plan. EPL/Duke University (Pub.): 64.
- Berg, A.A., Famiglietti, J.S., Walker, J.P., Houser, P.R., 2003. Impact of bias correction to reanalysis products on simulations of North American soil moisture and hydrological fluxes. *J. Geophys. Res.-Atmosph.* 108 (D16).
- Chavez, P.S., 1996. Image-based atmospheric corrections revisited and improved. *Photogram. Eng. Remote Sens.* 62 (9).
- Cosgrove, B.A. et al., 2003. Real-time and retrospective forcing in the North American Land Data Assimilation System (NLDAS) project. *J. Geophys. Res.-Atmosph.* 108 (D22).
- Decker, M. et al., 2012. Evaluation of the reanalysis products from GSFC, NCEP, and ECMWF using flux tower observations. *J. Clim.* 25 (6), 1916–1944.
- Dozier, J., 1980. A clear-sky spectral solar radiation model for snow-covered mountainous terrain. *Water Resour. Res.* 16 (4), 709–718.
- Dozier, J., Frew, J., 1990. Rapid calculation of terrain parameters for radiation modeling from digital elevation data. *IEEE Transact. Geosci. Remote Sens.* 28 (5), 963–969.
- Dubayah, R., Loehel, S., 1997. Modeling topographic solar radiation using GOES data. *J. Appl. Meteorol.* 36, 141–154.
- Dubayah, R., Paul, M., 1995. Topographic solar radiation models for GIS. *Int. J. Geograph. Inform. Syst.* 9 (4), 405–419.
- Frew, J.E.J., 1990. The Image Processing Workbench, UNIVERSITY OF CALIFORNIA, Santa Barbara. [Doctor].
- Gao, L., Bernhardt, M., Schulz, K., 2012. Elevation correction of ERA-Interim temperature data in complex terrain. *Hydrol. Earth Syst. Sci.* 16 (12), 4661–4673.
- Hay, L.E., Clark, M.P., 2003. Use of statistically and dynamically downscaled atmospheric model output for hydrologic simulations in three mountainous basins in the western United States. *J. Hydrol.* 282 (1–4), 56–75.
- Kumar, S., Merwade, V., 2011. Evaluation of NARR and CLM3.5 outputs for surface water and energy budgets in the Mississippi River Basin. *J. Geophys. Res.-Atmosph.*, pp. 116.
- Lenters, J.D., Coe, M.T., Foley, J.A., 2000. Surface water balance of the continental United States, 1963–1995: regional evaluation of a terrestrial biosphere model and the NCEP/NCAR reanalysis. *J. Geophys. Res.-Atmosph.* 105 (D17), 22393–22425.
- Lettau, H.H., 1959. Wind profile, surface stress and geostrophic drag coefficients in the atmospheric surface layer. *Adv. Geophys.* 6, 241.
- Maurer, E.P., O'Donnell, G.M., Lettenmaier, D.P., Roads, J.O., 2001. Evaluation of the land surface water budget in NCEP/NCAR and NCEP/DOE reanalyses using an off-line hydrologic model. *J. Geophys. Res.-Atmosph.* 106 (D16), 17841–17862.
- Mast, M.A., Turk, J.T., 1999. Environmental characteristics and water quality of Hydrologic Benchmark Network stations in the Eastern United States, 1963–95: U.S. Geological Survey Circular 1173-A, 158 p.
- Mesinger, F. et al., 2006. North American regional reanalysis. *Bull. Am. Meteorol. Soc.* 87 (3), 343–360.
- Mitchell, K.E. et al., 2004. The multi-institution North American Land Data Assimilation System (NLDAS): Utilizing multiple GCIP products and partners in a continental distributed hydrological modeling system. *J. Geophys. Res.-Atmosph.* 109 (D7).
- Ngo-Duc, T., Polcher, J., Laval, K., 2005. A 53-year forcing data set for land surface models. *J. Geophys. Res.-Atmosph.* 110 (D6).
- Nogueira, M., Barros, A., 2014a. The Integrated Precipitation and Hydrology Experiment - Hydrologic Applications for the Southeast US (IPHEX-H4SE) Part III: High-Resolution Ensemble Rainfall Products. Report EPL-2013-IPHEX-H4SE-3, EPL/Duke University (Pub.): 80.
- Nogueira, M., Barros, A.P., 2014b. The non-convective/convective structural transition in stochastic scaling of atmospheric fields. *J. Geophys. Res.-Atmosph.* 119. <http://dx.doi.org/10.1002/2014JD022548>.
- Nogueira, M., Barros, A.P., 2015. Transient stochastic downscaling of quantitative precipitation estimates for hydrological applications. *J. Hydrology* 529, 1407–1421. <http://dx.doi.org/10.1016/j.jhydrol.2015.08.041>.
- Pinker, R.T. et al., 2003. Surface radiation budgets in support of the GEWEX Continental-Scale International Project (GCIP) and the GEWEX Americas Prediction Project (GAPP), including the North American Land Data Assimilation System (NLDAS) Project. *J. Geophys. Res.-Atmosph.* 108 (D22).
- Roads, J., Betts, A., 2000. NCEP-NCAR and ECMWF reanalysis surface water and energy budgets for the Mississippi River basin. *J. Hydrometeorol.* 1 (1), 88–94.
- Schaaf, C.B. et al., 2002. First operational BRDF, albedo nadir reflectance products from MODIS. *Remote Sens. Environ.* 83 (1–2), 135–148.
- Schomburg, A., Venema, V., Lindau, R., Ament, F., Simmer, C., 2010. A downscaling scheme for atmospheric variables to drive soil-vegetation-atmosphere transfer models. *Tellus B* 62 (4), 242–258.
- Schroeder, T.A., Hember, R., Coops, N.C., Liang, S.L., 2009. Validation of solar radiation surfaces from MODIS and reanalysis data over topographically complex terrain. *J. Appl. Meteorol. Climatol.* 48 (12), 2441–2458.
- Sun, X., Barros, A.P., 2010. An Evaluation of the Statistics of Rainfall Extremes in Raingauge Observations, and Satellite-based and Reanalysis Products Using Multifractals. *J. Hydromet.* <http://dx.doi.org/10.1175/2009JHM1142.1>.
- Tao, J., Wu, D., Gourley, J., Zhang, S.Q., Crow, W., Peters-Lidard, C., Barros, A.P., 2016. Operational hydrological forecasting during the IPHEX-IOP campaign- meet the challenge. *J. Hydrol.* 541, 434–456. <http://dx.doi.org/10.1016/j.jhydrol.2016.02.019>.
- Tao, J., Barros, A., 2014a. Coupled prediction of flood response and debris flow initiation during warm-and cold-season events in the Southern Appalachians, USA. *Hydrolog. Earth Syst. Sci.* 18 (1), 367–388.
- Tao, J., Barros, A., 2014b. The Integrated Precipitation and Hydrology Experiment. Part I: Quality High-Resolution Landscape Attributes Datasets. Report EPL-2013-IPHEX-H4SE-1, EPL/Duke University (Pub.): 60.
- Tao, J., Barros, A., 2014c. The Integrated Precipitation and Hydrology Experiment. Part II: Atmospheric Forcing and Topographic Corrections. Report EPL-2013-IPHEX-H4SE-2, EPL/Duke University (Pub.): 80.
- Tao, J., Barros, A.P., 2013. Prospects for flash flood forecasting in mountainous regions – an investigation of Tropical Storm Fay in the Southern Appalachians. *J. Hydrol.* 506, 69–89.
- Wang, A.H., Zeng, X.B., 2012. Evaluation of multireanalysis products with in situ observations over the Tibetan Plateau. *J. Geophys. Res.-Atmosph.*, pp. 117.
- Wilson, A.M., Barros, A.P., 2014. An investigation of warm rainfall microphysics in the southern appalachians: orographic enhancement via low-level seeder-feeder interactions. *J. Atmosph. Sci.* 71 (5), 1783–1805.
- Wilson, A.M., Barros, A.P., 2015. Landform controls on low level moisture convergence and the diurnal cycle of warm season orographic rainfall in the southern appalachians. *J. Hydrol.* 531 (2), 475–493. <http://dx.doi.org/10.1016/j.jhydrol.2015.10.068>.
- Xia, Y.L., et al., 2012a. Continental-scale water and energy flux analysis and validation for North American Land Data Assimilation System project phase 2 (NLDAS-2): 2. Validation of model-simulated streamflow. *J. Geophys. Res.-Atmosph.*, pp. 117.
- Xia, Y.L., et al., 2012b. Continental-scale water and energy flux analysis and validation for the North American Land Data Assimilation System project phase 2 (NLDAS-2): 1. Intercomparison and application of model products. *J. Geophys. Res.-Atmosph.*, pp. 117.
- Yildiz, O., Barros, A.P., 2007. Elucidating vegetation controls on the hydroclimatology of a mid-latitude basin. *J. Hydrol.* 333 (2–4), 431–448.
- Zhao, T., Guo, W., Fu, C., 2008. Calibrating and evaluating reanalysis surface temperature error by topographic correction. *J. Clim.* 21 (6), 1440–1446.